AlFeCoNi high entropy alloy fabricated by powder-bed arc additive manufacturing

Jingdan Zhang

Supervisor: Professor Xiaozhou Liao

Auxiliary supervisor: Professor Simon Ringer

A thesis submitted in fulfilment of the requirements for the degree of

Master of Philosophy

School of Aerospace, Mechanical and Mechatronic Engineering

The University of Sydney

30 December 2023

Declaration

This is to certify that to the best of my knowledge, the content of this thesis is my own work. This thesis has not been submitted for any degree or other purposes. I certify that the intellectual content of this thesis is the product of my own work and that all the assistance received in preparing this thesis and sources have been acknowledged.

Signature _____

Name Jingdan Zhang

Abstract

Additive manufacturing has received a lot of attention in recent years. Compared with traditional manufacturing technology, additive manufacturing has many irreplaceable advantages. In 3D printing technology, most technologies need to prepare materials in advance when printing high-entropy alloy materials, which greatly increases the cost and time of 3D printing. Therefore, powder-bed arc additive manufacturing (PAAM) technology is adopted. However, PAAM technology will cause the grain size of the material to be very large, leading to poor mechanical performance. Therefore, I utilize the eutectic reaction to reduce the grain size of the material to obtain excellent mechanical properties. Therefore, this project uses PAAM technology to prepare high-entropy alloys with excellent properties, and observes the microstructure of the materials to analyze the reasons for the excellent mechanical properties of the materials. Therefore, this project will conduct a comprehensive study of the material's microstructure using advanced scanning electron microscopy (SEM). These advanced methods can observe the microstructure of materials during 3D printing.

In our project, the ductility of materials produced through PAAM technology increased by 8.5% compared to materials produced using traditional casting technology. Since 3D printing is a directional solidification method, the unique dendritic microstructure of directional solidification appears, which improves the ductility of the material. Due to certain technical problems in PAAM technology, there will be Al elements in the printing process. The loss results in the material not exhibiting a perfect lamellar-like microstructure at the top. At the same time, the content of the soft $L1_2$ phase at the top of the sample is approximately 72.3%. This phenomenon also leads to a decrease in the strength of the material, which is 90MPa lower than that of materials produced by traditional casting technology.

The first chapter of this paper introduces the research background of the project and the problems that the project wants to solve. The second chapter is a literature review,

which introduces the research progress in the same field. Chapter 3 explains the reasons for choosing $Al_{0.95}CoFeNi_{2.05}$ and the printing parameters and how the samples were prepared during the project. Chapter 4 presents the experimental results of the research obtained using the methods described above. These data are used to fully explore this material at different stages from macro to micro. Reasons for the results are discussed. Most importantly, this chapter summarizes the relationship between material microstructure and mechanical properties based on all these data. The final chapter sets out the main observations and conclusions of the project and points out some issues for further research.

Acknowledgements

The successful completion of this project would not have been possible without the guidance of my supervisor, the support of colleagues and friends, and the unwavering love of my family. This is the moment to express my heartfelt gratitude.

First and foremost, I extend my sincere thanks to my supervisor, Professor Xiaozhou Liao. His academic attitude and professionalism have profoundly influenced my performance during my MPhil studies. Even amid the challenges of the ongoing epidemic in 2022, he has ardently guided every step of the project with enthusiasm and confidence, serving as my role model.

Special appreciation goes to my co-supervisor, Professor Simon Ringer, whose support was invaluable throughout my MPhil research. My gratitude extends to Dr. Bosheng Dong and Prof. Huijun Li of the University of Wollongong for their help in producing HEA samples. Their support greatly contributed to the success of my experimental design.

I would like to acknowledge Dr. Hongjian Wang from the School of Aerospace, Mechanical and Mechatronic Engineering for technical assistance with mechanical tensile testing and sample density. My thanks also go to Dr. Vijay Bhatia and Dr. Huma Bilal from the Australian Center for Microscopy and Microanalysis (ACMM) for providing training on SEM instrumentation, and to Dr. Hongwei Liu and Dr. Jiangtao Qu from the ACMM for their guidance in transmission electron microscopy. Additionally, Dr. Samuel Duyker of Sydney Analytical deserves appreciation for providing training in X-ray diffraction.

Gratitude is extended to some members of Professor Liao's team, for their crucial technical assistance with microscopic characterization. I'm particularly thankful to Dr. Hao Wang for his insightful discussions and friendly help during my MPhil studies. Special thanks to Mr. Shunyao Du and Mr. Jinqiao Liu for their strong support and

companionship.

Last but not least, I express profound appreciation to my beloved family for their unwavering love and support throughout my academic journey.

Note: This paper was edited by ChatGPT, and the editorial intervention adheres to Australian Standards of Editorial Practice D and E standards.

List of Acronyms and abbreviations

AM	Additive manufacturing
BSE	Backscattered electrons
DLP	Digital Light Processing
DMLS	Direct Metal Laser Sintering
EBAM	Electron Beam Additive Manufacturing
EBM	Electron Beam Melting
EBSD	Electron backscattered diffraction
EDS	Energy-dispersive X-ray spectroscopy
FCC	Face-centered cubic
FDM	Fused Deposition Modeling
GBS	Grain boundary sliding
HEA	High entropy alloy
H-P	Hall-Petch
IPF	Inverse pole figure
IPF-Z	Inverse pole figure along the Z direction
LENS	Laser Engineered Net Shaping
LOM	Laminated Object Manufacturing
MJF	Multi Jet Fusion
MSLA	Masked Stereolithography
PAAM	Powder-bed arc additive manufacturing
SAD	Selected area diffraction
SE	secondary electrons
SEM	Scanning electron microscopy
SLA	Stereolithography
SLM	Selective Laser Melting
SLS	Selective Laser Sintering
STEM	Scanning transmission electron microscopy

TEM	Transmission electron microscopy
UC	Ultrasonic Consolidation
XRD	X-ray diffraction

Table of contents

Chapter 1: Introduction

1.1 Background and motivation

Additive manufacturing, commonly known as 3D printing, represents a rapid prototyping technology that has witnessed widespread adoption globally in recent years. Its application spans various fields such as agriculture, healthcare, automotive, and aerospace, offering extensive customization and manufacturing capabilities. Unlike traditional manufacturing methods, 3D printing involves minimal constraints, such as the absence of fixtures and tool interference, allowing for unparalleled flexibility. This technology facilitates the direct modeling and design of overall structures and complex features based on specific functional requirements. Additionally, 3D printing allows for the optimization of structural forms, resulting in relatively lighter materials and reduced weight. The simplified 3D printing process, in comparison to conventional methods, not only resolves issues related to challenging processing and part deformation but also enhances the efficiency of raw material utilization.

Why choose the way of PAAM. Because in the traditional way of 3D printing high-entropy alloys, I need to use traditional processes to make a very large high-entropy alloy in advance. The alloy was remelted five times to ensure chemical homogeneity of the sample. The alloy is then turned into a high-entropy alloy powder using gas atomize. The high-entropy alloy powder is then 3D printed. This material manufacturing process will cost a lot of time and money.

But with PAAM's technology, I can use a mechanical way of mixing powders. In the process of manufacturing high-entropy alloys, I only need to put the powder of each element into the instrument according to the required rate. Since the molten pool of this technology is very large, there is enough space for element homogenization. Therefore, this technology greatly reduces the time and cost of material manufacturing.

High-entropy alloys (HEAs), initially conceptualized by Yeh and Cantor et al. [1,2], have

garnered significant attention owing to their fascinating metallurgical philosophies and attractive physical and mechanical properties [1−6]. They adopt a multicomponent alloying concept, a departure from the conventional metallurgical design relying on one or two principal elements [1,2], to meet specific application requirements. Despite incorporating multiple principal elements, these alloys commonly solidify into straightforward crystal types like face-centered-cubic (FCC), body-centered-cubic (BCC), and hexagonal-close-packed (HCP) solid-solution structures or their ordered derivatives (such as $L1_2$ and B2) [1,2].

In the realm of high-entropy alloys (HEAs), those with an FCC (face-centered cubic) structure are known for their ductility, yet they often fall short in terms of strength. On the other hand, HEAs that possess BCC (body-centered cubic) or HCP (hexagonal close-packed) structures exhibit remarkable strength, but this comes with an increased tendency towards brittleness, a trade-off that is significant in material science [7−10]. Furthermore, these conventional HEAs face challenges in casting processes and are prone to uneven distribution of elements (composition segregation), which undermines their potential for outstanding performance across a variety of engineering applications. This segregation issue, in particular, can significantly impact the alloy's mechanical properties and its ability to leverage the benefits of its multi-component nature, an aspect critical for diverse applications in sectors like aerospace and automotive industries where material performance is paramount [7−10].

In response to these challenges, Lu et al. introduced $AlCoCrFeNi_{2.1}$ eutectic high-entropy alloys (EHEAs) based on the conventional eutectic concept. These alloys not only exhibit good liquidity and castability but also possess a remarkable strength–ductility synergy [11]. Subsequently, various EHEAs have been designed and successfully prepared, featuring different as-cast constituent phases and mechanical properties. Among the reported EHEAs, those with FCC/Laves structures typically display high strength but limited tensile plasticity. In contrast, FCC/BCC-structured EHEAs and their ordered derivatives are identified for their favorable combination of strength and ductility [12−14].

To address these challenges, Lu and colleagues pioneered the use of $AlCoCrFeNi_{2.1}$ eutectic high-entropy alloys (EHEAs), drawing on traditional eutectic principles. These EHEAs stand out for their excellent fluidity and ease of casting, coupled with an impressive synergy of strength and ductility [11]. This breakthrough led to the development and successful fabrication of various EHEAs, each characterized by unique cast constituent phases and mechanical attributes. Among these, the EHEAs with FCC/Laves structures are noted for their high strength, albeit with a compromise in tensile plasticity. Conversely, EHEAs structured with FCC/BCC phases, as well as their ordered variants, have garnered attention for their optimal balance of strength and ductility, marking a significant advancement in the field [12–14].

The superior performance of the latter EHEAs is attributed to a fine lamellar composite microstructure, high phase-interface density, and the coordinated co-deformation of alternate hard and ductile phases [8,14,15]. Therefore, the research goal of this project is to use PAAM technology to study the mechanical properties of high-entropy alloys that undergo eutectic reactions to produce FCC and BCC dual-phase structures.

1.2 Outstanding issues and the research objectives

While offering numerous advantages, 3D printing is not without limitations. Certain 3D printing technologies can be expensive [16], leading to a notable increase in material expenses during manufacturing.

The PAAM instrument is shown in Fig 1-1. The printed sample is shown in Fig 1-2. There are also some problems with this technology. Because of the large molten pool in manufacturing, although chemical uniformity can be guaranteed, it also leads to very large grain growth of the material. Large Grain size leads to a reduction in the mechanical properties of the material, so the grain size should be reduced. We chose the eutectic reaction to refine the grains. In this way, the strength and plasticity of the sample can be improved.

When I print the material and perform microstructural characterization, the phase

content will vary due to the different thermal cycles of the 3D printed layers. Both the growth of the dual phase and the microstructural evolution of the material during printing can affect the mechanical properties of the material. So, this project research focuses on the effect of the microstructure of the material on the mechanical properties.

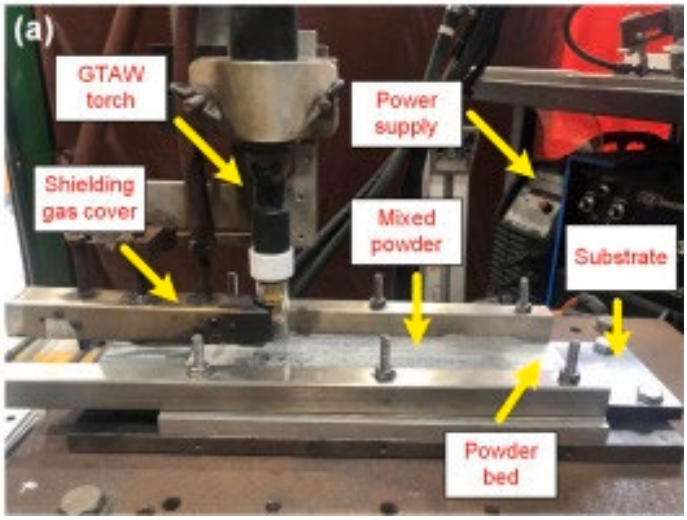

Fig 1-1. PAAM device

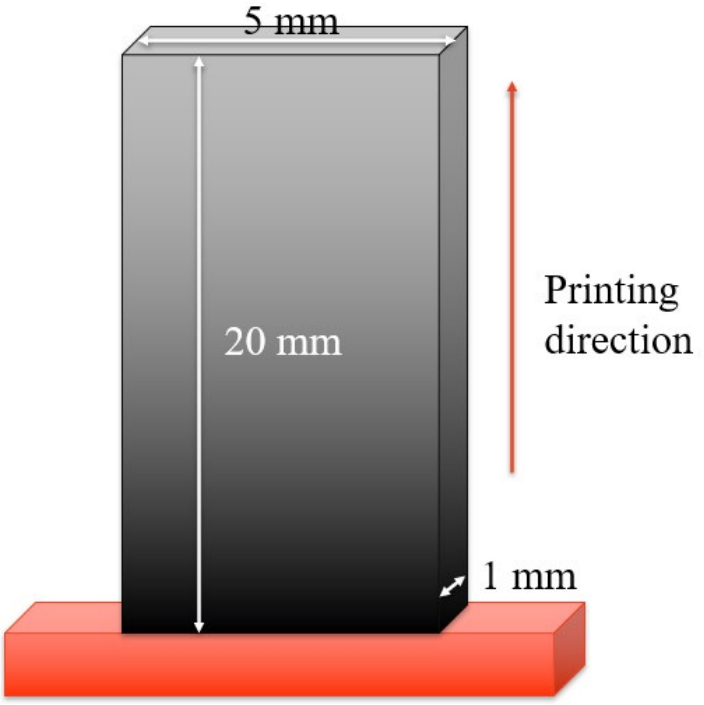

Fig 1-2. Schematic diagram of sample structure produced using PAAM technology.

Chapter 2: Literature Review

2.1 Additive manufacturing and its challenges

Additive manufacturing technology, commonly known as 3D printing, is a rapid prototyping technology. It builds objects by printing layers of bondable materials, such as powdered metal or plastic, based on digital model files (CAD) [1,2,4] . Due to its revolutionary significance in the industrial sector, 3D printing technology is also referred to as "manufacturing technology with industrial revolution significance." Unlike traditional manufacturing methods, 3D printing eliminates constraints like fixtures and tool interference. This enables the modelling and design of overall structures and complex features directly from a functional perspective, tailored to specific requirements. Furthermore, 3D printing optimizes the structural form and reduces the weight of materials, making them relatively lighter. The 3D printing process is also simplified compared to traditional methods, while improving the utilization rate of raw materials. Overall, it addresses the challenges associated with traditional processing, such as complex part processing and preserving part information. Additionally, 3D printing allows for the creation of complex shapes and surfaces that are unachievable with traditional processes [3]. Over the past few years, 3D printing has gained widespread adoption worldwide, particularly in agriculture, healthcare, automotive industry, and aerospace sectors, enabling extensive customization and manufacturing capabilities [5,6] . According to American Society for Testing and Materials (ASTM), additive manufacturing is classified into seven processes: VAT Photopolymerization, Material Jetting, Binder Jetting, Material Extrusion, Powder Bed Fusion, Sheet Lamination, and Direct Energy Deposition [7]. With the advancements in technology, the range and types of 3D printing methods have been gradually expanding, as summarized in Table 2-1 below.

Table 2-1. The 7 main 3D printing technologies that are popular today

3D Printing Process				
Material Extrusion	Fused Deposition Modeling (FDM)			
Vat Polymerization	Stereolithography (SLA)	Digital Light Processing (DLP)	Masked Stereolithography (MSLA)	
Powder Bed Fusion	Selective Laser Sintering (SLS)	Direct Metal Laser Sintering (DMLS)/Selective Laser Melting (SLM)	Electron Beam Melting (EBM)	Multi Jet Fusion (MJF)
Material Jetting	Material Jetting (MJ)		Drop on Demand (DOD)	
Direct Energy Deposition	Electron Beam Additive Manufacturing (EBAM)	Laser Engineered Net Shaping (LENS)	Cold Spray	
Binder Jetting	Sand Binder Jetting	Metal Binder Jetting	Plastic Binder Jetting	
Sheet Lamination	Laminated Object Manufacturing (LOM)		Ultrasonic Consolidation (UC)	

For material manufacturing, the initial approach often involves using traditional machining techniques to produce parts. These techniques primarily consist of subtractive machining and isometrical machining. Subtractive machining relies on mechanical external force, utilizing tools harder than the material being processed to remove excess material. It encompasses processes such as turning, milling, planning, grinding, and drilling. Conventional machining methods come with a host of challenges such as suboptimal working conditions, intricate procedural demands, extended production times, difficulties in adjusting designs, elevated costs for small-scale production, and the need for highly skilled operators. These factors hinder the ability of traditional machining techniques to keep pace with the swift production needs essential for the rapid iteration of part development. Beyond subtractive machining, the two main isometrical machining processes are casting and forging. However, casting has its limitations, particularly in terms of lower mechanical strength and the potential for uncontrolled internal defects, making it less suitable for parts requiring high mechanical integrity. Conversely, forging stands out as a key technique in the creation of load-bearing components for various mechanical devices, owing to its ability to produce parts with superior mechanical properties and reliability. Die forgings closely

resemble the final product and require minimal additional processing. However, the design and manufacturing cycle of dies pose significant cost pressures when incorporating structural design changes [3].

2.2 Importance of reducing the size of additively manufactured parts

In metal fabrication, one persistent challenge is achieving sufficient metal strength, which is often hindered by large grain sizes and limited control over grain shape [17].

Reducing the grain size of a metal results in a larger total area of grain boundaries and an increased number of dislocation barriers [18−27]. Refining grains has consistently proven to be an effective method for enhancing the strength of polycrystalline materials [28−35]. According to dislocation theory, grain boundaries serve as hindrances to dislocation movement. To induce shear deformation in adjacent grains under external forces, a significant stress concentration must occur at grain boundaries, leading to grain refinement and the creation of more grain boundaries. If the grain boundary structure remains unchanged, a higher external force is needed to generate dislocation accumulation, ultimately strengthening the material. The Hall-Petch relationship is derived from the misplacement product model [17].

Regarding the role of grain size, it can be elucidated from the perspective of dislocations within crystal defects. Dislocations are distributed in three locations, and the line segments of the dislocation network on the slip plane can act as dislocation sources. Under stress, dislocation sources continuously release dislocations, causing crystal slippage. During dislocation movement, they must overcome the obstacles of the dislocation network. As dislocations reach grain boundaries, they encounter additional obstacles, requiring overcoming the resistance between grains for deformation to transfer from one grain to another. This process leads to the material yielding. Thus, the yield strength of metal depends on factors such as the force needed to move the dislocation source and the resistance offered by the dislocation network and grain

boundaries. In the same volume of metal, finer grains result in more grain boundaries and obstacles, requiring increased external force for crystal slippage. Consequently, smaller grain sizes correspond to higher material yield limits.

Smaller grain size helps improve the material's plasticity and toughness [36−39]. This is due to the increased number of grains within the same area. During the deformation process, a greater number of grains participate in the deformation, promoting more uniform deformation behavior. As a result, the material can undergo significant plastic deformations prior to fracture, requiring more energy during the deformation process. Ultimately, this leads to improved plasticity and toughness of the material [36−39].

2.3 Grain size reduction techniques in additive manufacturing

Reducing grain size offers multiple advantages and is of great importance in the preparation of crystalline materials. The first advantage is the enhancement of strength and hardness [40−44]. Smaller grains typically contain more grain boundaries, which impede the propagation of dislocations, thereby increasing the material's strength and hardness. Additionally, smaller grains restrict dislocation movement, making it more challenging for the material to deform and thereby enhancing its resistance to deformation.

The second benefit of smaller grains is the improvement in plasticity and toughness [22,40,45−47]. Smaller grain sizes reduce the slip distance of dislocations, which, in turn, decreases the plastic strain of the material. However, they may also increase the number of grain boundaries, facilitating the absorption and distribution of energy, and ultimately improving the material's toughness and resistance to fracture.

Finally, smaller grains contribute to the microstructural homogeneity of the material [40,48−50]. They allow for a more uniform distribution of structures throughout the material, reducing material heterogeneity and thereby enhancing its consistency and

reliability. As a result, scientists and engineers employ various methods to control and optimize grain size to meet the requirements of different applications.

In the context of grain reduction in the 3D printing process, there are five commonly used methods to reduce grain size. The first involves rapid solidification rates [51,52]. During 3D printing, materials tend to solidify at a faster rate than in traditional methods, limiting the time available for crystals to grow and reducing grain size.

The second method is the utilization of refiners, which act as catalysts during the crystal growth process, accelerating the formation of crystals [28,53−57]. Refining agents can introduce substantial bending strains at the crystal interface, effectively restricting grain growth and maintaining small grain sizes.

The third method involves variations in the cure rate [58]. Due to factors like heat conduction during 3D printing, different areas may experience varying curing rates, resulting in different rates of crystal formation and more grain boundaries in the structure, leading to reduced grain size.

The addition of specific alloying elements to the material is the fourth method [59−61]. Some elements can create a unique interface structure near the grain boundary, restricting crystal growth and reducing grain size.

The fifth approach is heating treatment control [58,62,63]. After 3D printing, the size of crystals can be adjusted by precisely controlling the temperature and time during the heat treatment process. Through appropriate annealing processes, grains can be further refined to enhance material performance.

Another method is through eutectic and eutectoid reactions [64−67]. Eutectic reactions involve the simultaneous solidification of two or more phases, which limits grain growth and forms interlaced lath or columnar structures with more grain boundaries, ultimately reducing grain size. Eutectoid reactions introduce new phases near grain boundaries, hindering crystal growth and effectively reducing grain size.

In my project, I have chosen to reduce grain size through eutectic reactions to enhance

the mechanical properties of the material.

2.4 Eutectic reactions as a method for grain size reduction

The term "eutectic reaction" refers to the co-solidification of two or more components in an alloy at a specific temperature, resulting in the formation of phases in specific proportions. These phases are typically arranged in alternating lath-like, columnar, or granular structures, collectively forming a eutectic structure. The occurrence of a eutectic reaction is intricately involved in the solidification and phase transition processes of substances. At specific temperatures, the components in the alloy adopt different crystal structures in the solid state. These structures generally consist of two or more phases that solidify simultaneously at the eutectic point's temperature. During the solidification process, the different phases interlace to create lath-like, columnar, or granular morphologies, ultimately resulting in the formation of a eutectic structure.

Eutectic reactions often lead to the development of specific microstructures within the material, which significantly impact its performance and properties. Common types of eutectic structures include Lamellar Eutectic, Cellular Eutectic, Spherical Eutectic, and Peritectic Network.

1. Lamellar Eutectic: This structure consists of parallel laths, with each lath representing a different crystal phase. Lath eutectics are typically found in high-entropy alloys and other alloy systems, and they exert a significant influence on the mechanical properties and corrosion resistance of materials [68].

2. Cellular Eutectic: The cellular eutectic structure comprises numerous cellular units, each containing a core crystalline phase surrounded by another phase. Cellular eutectics are commonly observed in specific alloys and affect the material's strength and thermal conductivity.

3. Spherical Eutectic: This structure is composed of spherical or granular crystal phases, with each spherical structure consisting of one or more crystal phases.

Spheroidal eutectics are often present in certain metal alloys and ceramics, influencing the material's strength and wear resistance.

4. Peritectic Network: The peritectic network presents a complex network morphology, featuring multiple interwoven crystal phases. Network eutectics are observed in high-entropy alloys and complex alloy systems, affecting high-temperature performance and corrosion resistance in materials.

Eutectic reactions play a role in reducing grain size through a phenomenon known as "interface-limited growth." When eutectic reactions occur, two or more phases solidify simultaneously, forming interdigitated structures that result in a higher density of grain boundaries. Grain boundaries serve as impediments to crystal growth, as crystals cease to grow near these boundaries, effectively limiting the size of the grains. Additionally, grain boundaries typically possess higher energy, and crystals are influenced by this energy when growing near them. The grains of the lath, columnar, or granular phases within the eutectic structure cease their growth near the grain boundaries, contributing to the reduction of grain size.

Furthermore, eutectic reactions can interact to further constrain growth. Interactions between different phases within the eutectic structure may impose limitations on grain growth rates, resulting in a reduction in grain size.

2.4.1 Advantages of eutectic reactions for grain size reduction

The eutectic reaction offers unique advantages and benefits over other methods for reducing grain size. Firstly, it provides a high degree of controllability. This reaction can be precisely manipulated by adjusting the alloy's composition and temperature, allowing for precise control of grain size.

Secondly, it leads to the formation of a heterogeneous structure. Eutectic reactions involve the creation of multiple phases, which can introduce complex structures near grain boundaries. These grain and phase boundaries can influence grain growth through

the interaction of dislocations and interfaces, thereby reducing grain size.

Furthermore, the eutectic reaction finds application in a wide range of materials systems, including metal alloys and ceramic alloys, enabling grain refinement in various material types and resulting in improved performance.

Another notable advantage is its energy efficiency. Eutectic reactions typically occur under the solid-state conditions of the alloy, making them relatively energy efficient. They often require less energy than some high-temperature processing methods.

Lastly, the eutectic reaction can simultaneously enhance material properties in multiple aspects, such as strength, hardness, plasticity, toughness, and electrical conductivity. This makes the material more suitable for specific engineering applications [69−74].

3D printing not only allows for the precise fabrication of complex-shaped objects but also, when combined with high-entropy alloys, opens up entirely new possibilities in materials science. In this study, the eutectic reaction was employed as a means of reducing grain size. By carefully controlling temperature and composition during the 3D printing process, materials can be guided to undergo eutectic reactions at the microscopic scale. This approach enables the formation of materials with complex microstructures during printing, resulting in superior mechanical properties, thermal conductivity, and corrosion resistance.

In the context of high-entropy alloys and eutectic reactions, 3D printing offers a completely new method for exploring and customizing material microstructures. By adjusting printing parameters and alloy composition during the 3D printing process, the occurrence of the eutectic reaction can be precisely controlled, tailoring the material's properties. This method can also overcome the challenges associated with achieving specific microstructures in traditional methods, such as the formation of eutectic phases of specific sizes, further enhancing material performance.

In conclusion, the combination of 3D printing, high-entropy alloys, and eutectic reactions holds great potential in the field of materials science. This innovative

approach can be used not only for manufacturing high-performance components but also for applications in the medical, aerospace, and other fields [75−82]. Through precise control and customization, materials with unique properties and microstructures can be created, opening up new possibilities for modern engineering and technology.

2.5 High entropy alloys

In recent years, high-entropy alloys (HEAs) have garnered considerable attention due to their distinctive features, encompassing variable compositions, intricate microstructures, and tunable material properties based on constituent elements [8−16,83−87]. A high-entropy alloy is characterized by the inclusion of five or more metals in roughly equal proportions [88]. As these alloys have the potential to yield materials with exceptional mechanical properties, they have become a focal point in materials science and engineering, drawing increasing interest from researchers and practitioners alike.

The concept of entropy (S) in high-entropy alloys is rooted in the principles set forth by Ludwig Boltzmann. Entropy, in this context, is a measure reflecting the degree of disorder or randomness at the atomic level within these alloys. According to Boltzmann's hypothesis, entropy is a linear function related to the logarithm of the number of microstates (distinct arrangements of atoms) that can occur in a given system. This relationship can be expressed through Boltzmann's entropy formula, which is a cornerstone in the field of statistical thermodynamics.

The formula for entropy in the context of high-entropy alloys is typically represented as:

$S_{mix} = R \ln(n)$

S_{mix}-high entropy of mixing

R-gas constant

n- concentration of mixing elements in equimolar ratio

According to recent research findings [89], when the value of n is equal to 5 (equimolar), the corresponding value of S_{mix} is determined to be 1.6R. However, in the case of high-entropy alloys produced under non-equimolar conditions, the value of S_{mix} is notably lower than that of equimolar HEAs, specifically at 1.5R. For high-temperature materials categorized as high-entropy alloys, their entropy typically hovers around 1.37R. The classification of alloys based on entropy values is delineated as follows: low entropy when $S_{mix} \leq R$, medium entropy alloy for $R \leq S_{mix} \leq 1.5R$, and high entropy alloy for $S_{mix} \geq 1.5$ [24]. This categorization is visually represented in Fig 2-1.

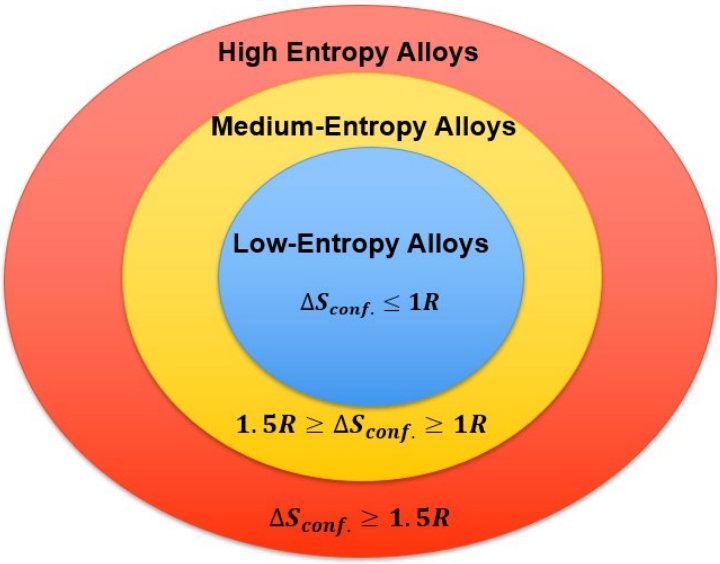

Fig 2-1. Classification of alloy based on mixing entropy [89]

2.6 Experimental techniques

During the research process, I chose XRD, SEM, and EBSD as the main research methods. The research method is shown in the fig 2-2.

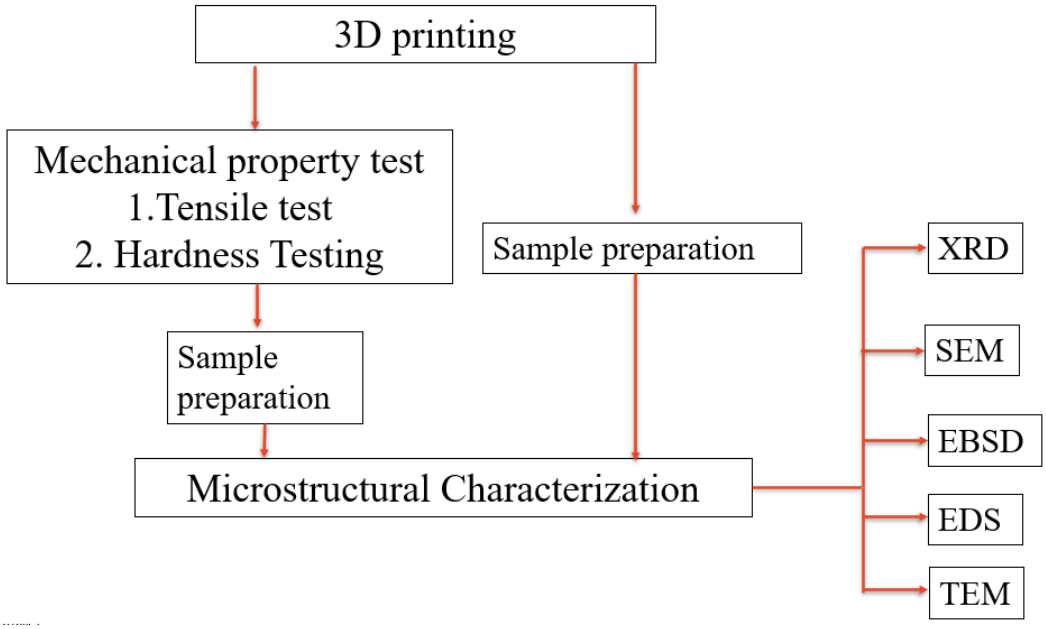

Fig 2-2. Schematic diagram of research process

2.6.1 X-ray Diffraction

X-rays, a type of electromagnetic wave, are distinguished by their exceptionally short wavelengths, which typically range from about 20 to 0.06 Ångströms. This characteristic allows them to penetrate materials that are relatively thin. When X-rays pass through these materials, they can induce phenomena such as fluorescence and gas ionization.

A significant milestone in the study of X-rays was achieved in 1912 by the German physicist Max von Laue. He proposed that crystals could act as three-dimensional diffraction gratings for X-rays. According to von Laue's hypothesis, when X-rays traverse a crystal lattice, they undergo diffraction, creating a pattern. This diffraction pattern, once captured on photographic film, can be analyzed to deduce the crystal's internal structure. This groundbreaking concept, for which von Laue received the Nobel Prize in Physics in 1914, laid the foundation for the field of X-ray crystallography [8].

This groundbreaking concept was further elucidated in 1913 by the British physicist Sir WH Bragg and his son Sir WL Bragg, who explained the phenomenon of X-ray

diffraction [90,91]. Fig 2-3 illustrates the X-ray diffraction (XRD) procedure. If X-rays of the same phase are scattered on adjacent atomic planes and can still be diffracted, the wave path difference between the two parallel rays must be an integer multiple of the wavelength [15]. This condition can be expressed as:

$$2d \sin \theta = n\lambda \qquad (2\text{-}1)$$

d represents the distance between two atomic planes in the scattering region

θ is the angle between the incident ray and the scattering planes

n is an integer (representing the order of the diffraction)

λ is the wavelength of the incident beam

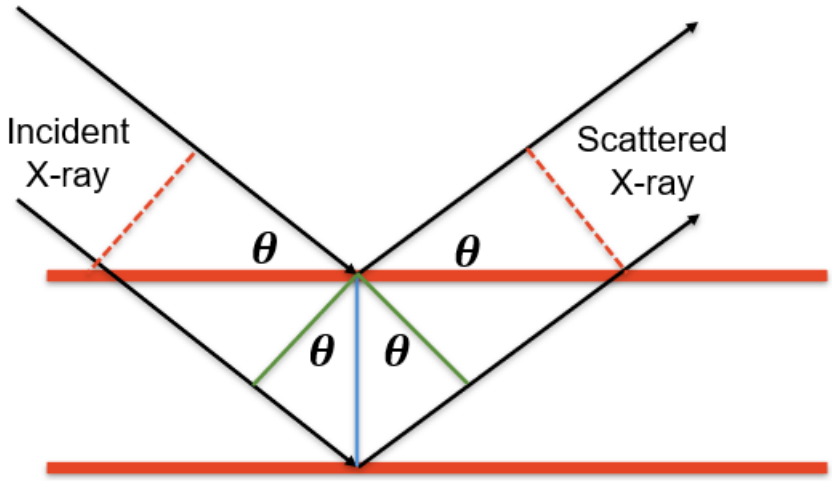

Fig 2-3. The schematic representation of Bragg diffraction illustrates X-rays being scattered at two adjacent atomic planes. The X-ray path difference diffracted in different planes is expressed as $2d \cdot \sin\theta$ [15].

In crystalline materials, distinct crystal planes correspond to different d values. When the X-ray wavelength is kept constant, as per Equation 2-1, diffraction occurs at a specific angle θ. Consequently, by systematically varying the angle across a broad range, one can identify the specific θ angles where diffraction occurs, facilitating the determination of lattice parameters. This fundamental principle has led to the development of the X-ray powder diffractometer, as depicted in the schematic diagram

in Fig 2-4 and Fig 2-5.

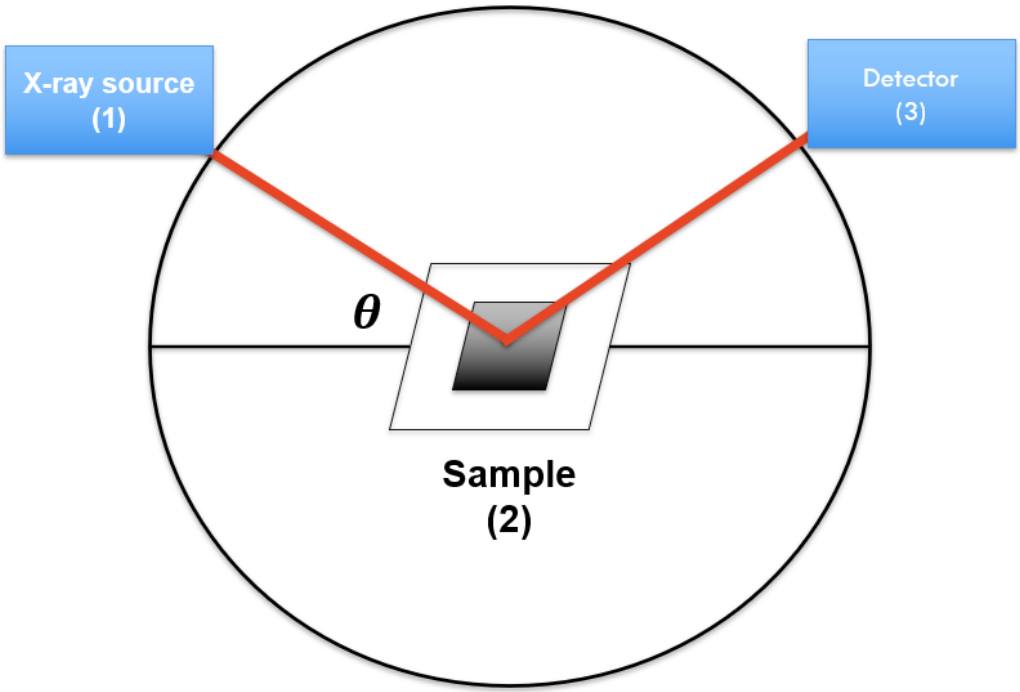

Fig 2-4. Schematic diagram of the working principle of XRD powder diffractometer [92]

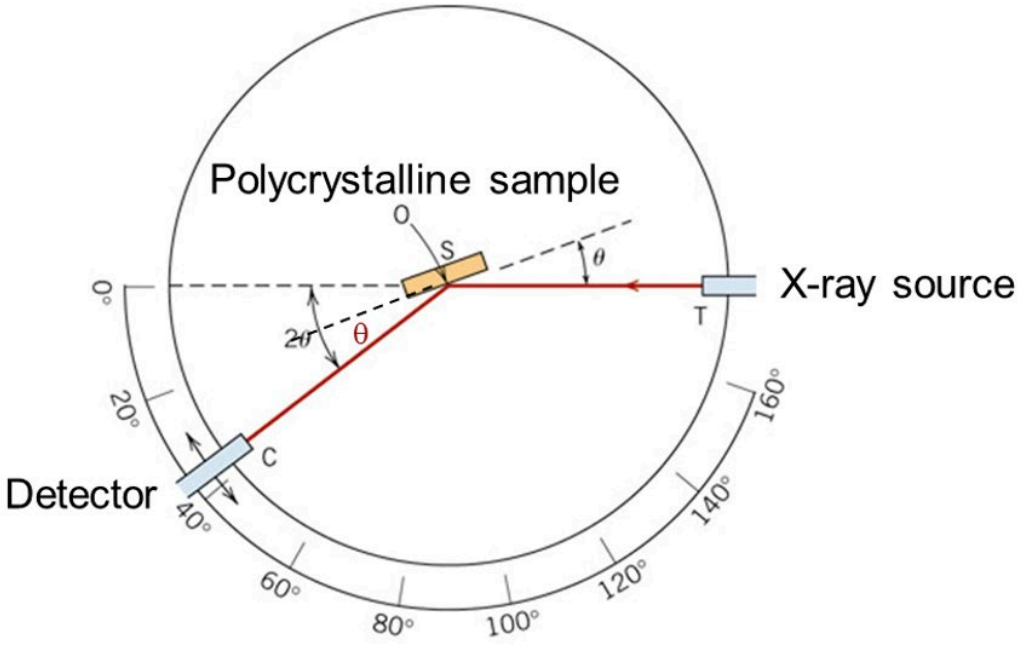

Fig 2-5. Theta-2theta relationship

The illustration portrays a sample securely placed within the cavity of an X-ray diffraction (XRD) instrument. Characteristic X-rays are directed towards the sample from the left. These X-rays undergo elastic scattering upon interacting with the sample's surface and are then detected by a receiver positioned on the right side of the apparatus. Both the X-ray source and the detector are aligned at a fixed angle relative to the horizontal plane. The setup is designed to vary this angle incrementally, scanning from one predetermined angle to another at a constant step rate.

The intensity of the detected X-rays changes as the angle of incidence varies. When the angle satisfies the criteria of Equation (2-1), a notable spike in signal intensity is observed at the detector on the right. This spike, or characteristic peak, is then plotted on a graph. By analyzing the angles at which these peaks occur and comparing them with those derived from standard samples, the crystallographic structure of the unknown sample can be elucidated. This process is supported by a comprehensive database of known crystal diffraction patterns, which serves as a reference for identifying and understanding the crystal structures of various materials. This database is a critical tool in X-ray crystallography, enabling researchers to match observed diffraction patterns with those of known substances, thus facilitating the identification of the crystalline structure of the sample under examination.

2.6.2 Scanning Electron Microscopy

To thoroughly examine the microstructural changes in crystals, a high level of spatial resolution is crucial. According to the Rayleigh criterion [93], this necessitates the use of a light source with an extremely short wavelength, a requirement that visible light cannot fulfill. A more effective approach involves the use of accelerated electrons, which have significantly shorter wavelengths. The wavelength of an electron is inversely related to its kinetic energy, which in turn is directly proportional to the acceleration voltage applied in the electron gun of the microscope. For example, in a typical transmission electron microscope (TEM) operating at an acceleration voltage of

200 keV, the theoretical limit of spatial resolution is calculated to be around 0.0015 nm. This resolution is significantly finer than the size of an atom. However, it's important to remember that this value is theoretical; in practice, imperfections in the magnetic lenses used for focusing the electrons lead to spherical aberrations, slightly degrading the actual spatial resolution. Despite this, TEMs are still capable of resolving atomic-scale structures, especially when additional corrective techniques are employed.

When the incident electron beam interacts with a sample, it generates a variety of detectable radiation signals. These include secondary electrons (SE), characteristic X-rays, visible light, backscattered electrons (BSE), Auger electrons, and both elastic and inelastic scattered electrons, as well as direct electrons. In Fig 2-6, these significant electron types are emphasized. Each category of electrons reveals different kinds of information: SE are used to map the surface topography of the sample, BSE provide insights into the atomic mass and grain orientation, characteristic X-rays are utilized for elemental identification, and direct electrons form two-dimensional projection images in transmission mode. Elastic and inelastic scattered electrons can be used to produce dark-field images, offering a way to distinguish between different orientations and elements in a manner somewhat akin to BSE. This diverse array of radiation signals has led to the development of sophisticated instruments designed to capture and analyze this rich trove of data, thereby advancing the field of materials science.

The Scanning Electron Microscope (SEM) operates on a mechanism involving the use of high voltage to accelerate electrons, which subsequently strike the sample's surface to produce images. The range of acceleration voltages is quite extensive, spanning from 1 keV to approximately 50 keV, depending on the specific application. Consequently, the electron energy in this microscopy doesn't have the ability to penetrate the sample, and the resulting radiation signal is distributed across the sample surface.

Following this, the electron beam is precisely focused by multiple sets of magnifying lenses and projected onto the surface of the sample. The operational principles of an SEM are illustrated in Fig 2-7. Once the sample's surface is struck, the collection of various types of detectors becomes necessary.

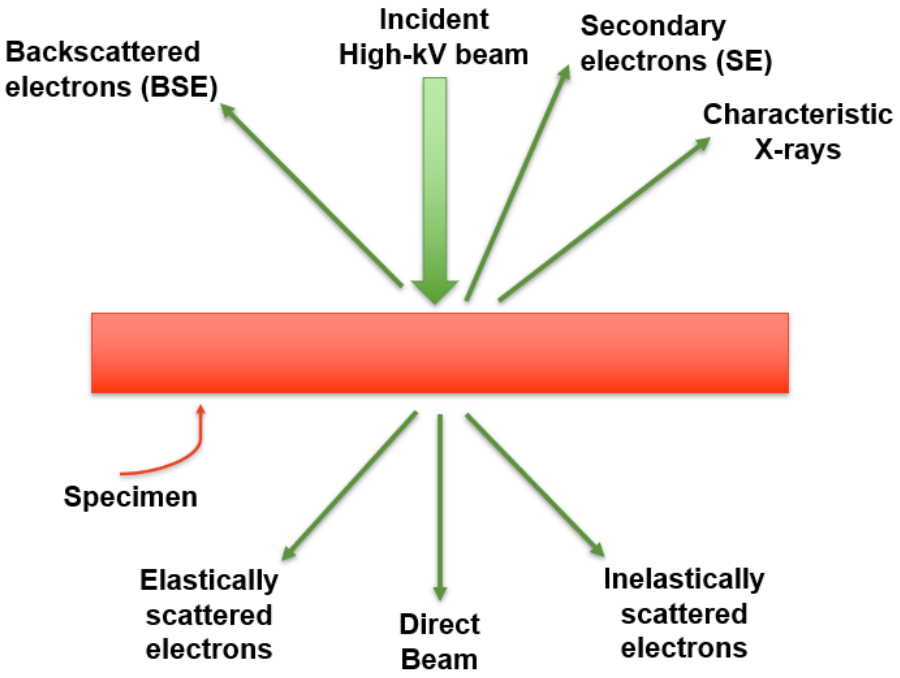

Fig 2-6. Schematic diagram of the main electronic signals introduced by the interaction between fast electrons and solid materials. The directions do not represent the physical direction of these radiations [94].

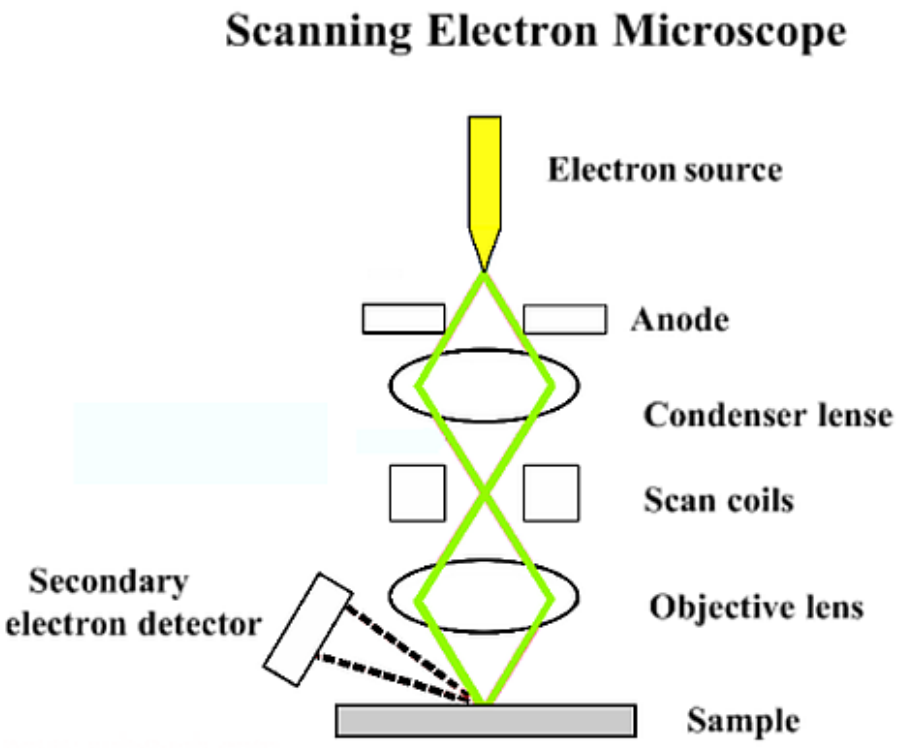

Fig 2-7. Schematic diagram of an SEM and detectors

2.6.2.1 Backscattered Electrons

Backscattered Electrons (BSE) are primarily elastic scattered electrons that interact with and are reflected by the nuclei of atoms on the surface of a material. In this elastic scattering process, the energy of the BSEs remains largely similar to that of the incident electrons from the beam. As a result, the intensity of the BSE signal is closely related to the characteristics and arrangement of the atomic nuclei at the surface. This relationship allows BSE imaging to effectively represent variations in relative atomic mass and grain orientation within the sample.

In BSE imaging (Fig 2-8.), the observed brightness in the image varies between grains of different orientations. This variation in brightness is particularly influenced by the atomic number of the elements: heavier elements, having larger nuclei, scatter more electrons and thus appear brighter in the image. This property of BSE makes it a valuable tool in materials science for examining the distribution of different elements and the orientation of grains in polycrystalline materials. BSE imaging, therefore, offers insightful information about the structural composition and phase distribution within a sample, contributing to a deeper understanding of its microstructural properties.

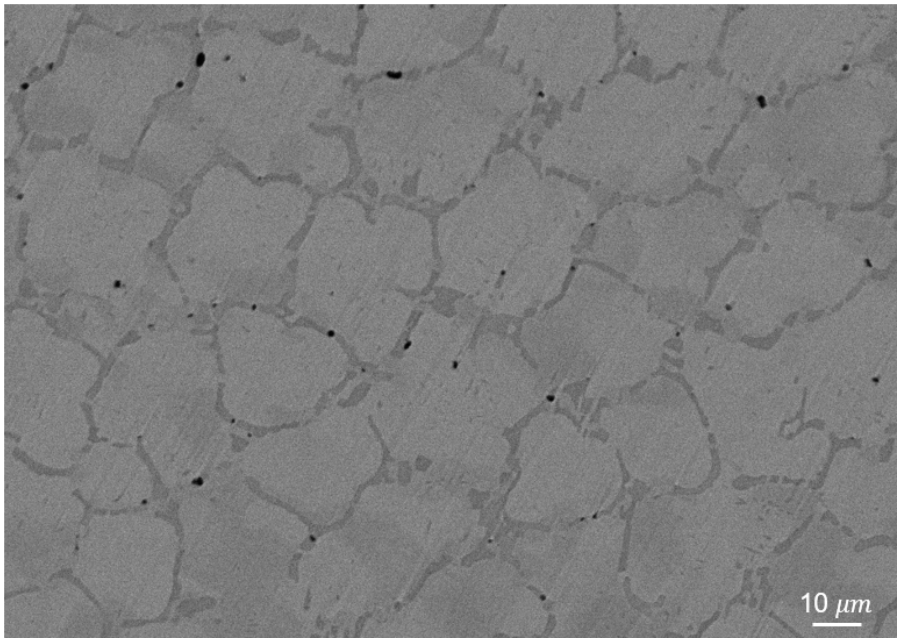

Fig 2-8. SEM-BSE image of $AlFeCoNi_{2.1}$

2.6.2.2 Secondary Electronics

The Secondary Electron (SE) detector is the most commonly utilized data collector in SEM (Fig 2-9). This detector captures the inelastic scattered electrons emitted due to the interaction between incident electrons and the outer electrons of surface atoms. Consequently, the energy of these electrons is significantly lower, typically in the range of 1-50 eV, necessitating a positive bias to draw them towards the collector and generate signals. These electrons carry rich information about surface topography [96]. It's noteworthy that, in the absence of a BSE collector, low-energy secondary electrons can be filtered by applying a slight negative bias in front of the SE detector, thereby allowing it to perform the function of a BSE collector [97].

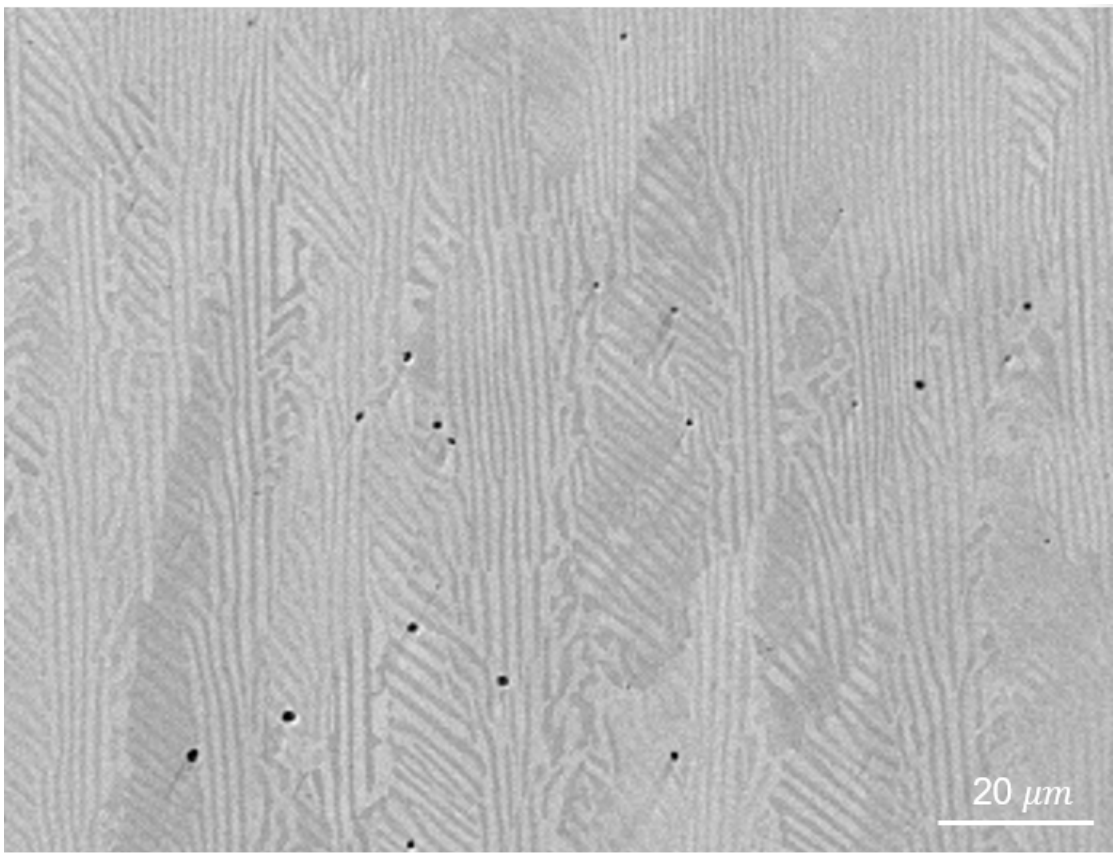

Fig 2-9. Photo schematic of high-entropy alloy SE.

2.6.2.3 Energy-Dispersive X-ray Spectroscopy

SEM-EDS (Scanning Electron Microscopy-Energy Dispersive X-ray Spectroscopy) analysis stands out as a non-destructive technique for analyzing sample materials. Unlike X-Ray Fluorescence (XRF), which can be conducted in situ without removing the sample, SEM-EDS requires the extraction of the sample. In this method, the sample is bombarded with electrons, leading to the emission of X-rays that are characteristic of the elements within the sample. These emissions translate into spectral peaks of varying intensities, forming a spectrum profile that aids in identifying the presence of various inorganic elements like lead, iron, copper, zinc, etc.

Next, the basic principles of energy-dispersive X-ray spectroscopy (EDS) of semiconductor detectors, typically silicon (Si), are presented. The process begins with the photoelectric absorption of an X-ray photon within the semiconductor's active volume. The photon's entire energy is transferred to a bound inner-shell atomic electron, which is then ejected with kinetic energy equal to the photon's energy minus the shell ionization energy. For silicon, these ionization energies are 1.838 keV for the Si K-shell and 0.098 keV for the Si L-shell.

The ejected photoelectron undergoes inelastic scattering within the Si crystal, leading to the generation of electron-hole pairs. This process occurs when bound outer-shell valence electrons are promoted to the conduction band, creating positively charged "holes" in the valence band. These free electrons move towards the anode at the rear surface of the EDS detector, while the positive holes drift in the opposite direction, resulting in the collection of charge.

Approximately 3.6 eV of energy is required to generate each electron-hole pair. The total number of charge carriers produced is directly proportional to the initial photon energy, as represented by the equation:

$$n = E_P / 3.6\ \text{eV} \qquad (2\text{-}2)$$

For example, a Mn K-L3 photon with an energy of 5.895 keV generates about 1638

electron-hole pairs, equivalent to a charge of 2.6×10^{-16}coulombs.

The detector is capable of responding to photon energies ranging from about 50 eV to 30 keV or more. Despite the name "energy dispersive," there's no actual dispersion in the sense of spectrometry, unlike in diffraction element spectrometers. This ability to respond to a wide range of photon energies allows for a comprehensive analysis of the elemental composition of the sample based on the emitted X-ray spectrum

The evolution of Energy Dispersive X-ray Spectrometry (EDS) has seen a significant shift from the original lithium-drifted silicon (Si(Li)-EDS) detectors to the more advanced silicon drift detectors (SDD-EDS). The Si(Li)-EDS, as depicted in Fig. x.1a, featured uniform electrodes on both the front and rear surfaces. However, in recent years, the SDD-EDS design has become more prevalent [98].

The SDD-EDS maintains the fundamental detection principles of its predecessor but introduces a refined electrode design. It includes a uniform front surface electrode and a complex arrangement of nested ring electrodes at the rear surface, culminating in a small central anode. This configuration of nested ring electrodes creates an internal "collection channel." This channel ensures that free electrons generated anywhere within the detector volume are efficiently guided towards the central anode for collection.

The process of accurately determining the energy of an incident X-ray photon involves measuring the charge deposited in the detector. This requires a highly sensitive and sophisticated electronic system, which operates largely under automatic computer control. The user has only limited control over a few parameters of this system.

The collected charge data forms the basis for constructing the EDS spectrum. This spectrum is displayed as a histogram, where the horizontal axis represents a range of energy bins, and the vertical axis indicates the number of photons falling into each bin. The EDS detection process, from a user perspective, functions like a "black box" that captures the X-ray photon, measures its energy, and then updates the spectrum histogram in the computer's memory, incrementing the count in the appropriate energy

bin.

EDS detectors are capable of measuring photon energies starting from a low threshold of about 0.05 keV, extending up to 30 keV or more, depending on the specific design of the detector. This wide range of detectable energies makes EDS a versatile tool for elemental analysis in various scientific and industrial applications.

2.6.2.4 Electron Backscatter Diffraction

To gain a comprehensive understanding of a material's physical properties, it is crucial to delve into its underlying crystallography. This comprehension forms the bedrock for revealing the intricate relationships between the material's structure and its behavior.

The introduction of electron backscattering diffraction (EBSD) equipment, along with its integration into commercial tools for phase identification and orientation determination, has opened up new vistas in the realms of microstructure, crystallography, and the physical properties of materials. This technological advancement has substantially enriched our insights into these aspects, leading to a profound understanding of materials.

EBSD, when applied within a scanning electron microscope (SEM), has evolved to serve two distinct purposes. The primary and older application involves the measurement of texture on a grain-by-grain basis. This technique provides what is known as the macrotexture of the sample [99]. An example of this approach is illustrated in Fig 2-10, which vividly displays the point-by-point orientation of a set of high entropy alloy. The color coding in the figure signifies their respective orientations.

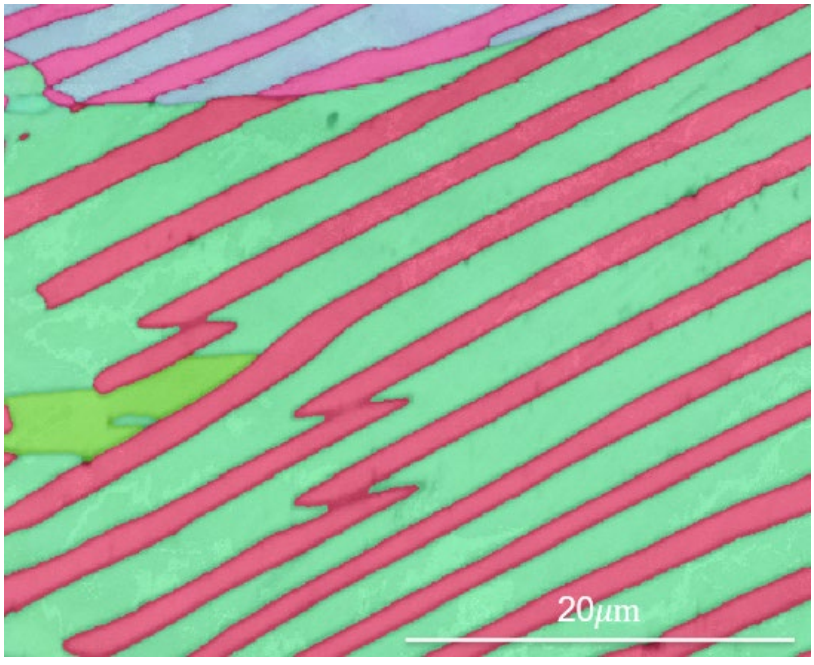

Fig 2-10. Inverse pole figure map of high entropy alloy

The second key application of Electron Backscatter Diffraction (EBSD) is its ability to identify or differentiate between crystalline phases at the micrometer or sub-micrometer scale [36]. EBSD is particularly adept at distinguishing between different crystal structures, thus greatly enhancing the analytical capabilities of the Scanning Electron Microscope (SEM). As a result, the SEM is now a versatile tool, not only for investigating sample morphology through secondary or backscattered electron imaging but also for analyzing chemical composition via Energy Dispersive Spectrometry (EDS) and exploring crystallography using techniques like Electron Channeling Contrast Imaging (ECCI) and EBSD.

Recent advancements in EBSD, specifically high-resolution EBSD (HR-EBSD) or high-angular-resolution EBSD, have enabled the determination of both elastic and plastic strains within microstructures. For those seeking a more comprehensive understanding of this advanced technique, additional literature is available [8,93].

Macrotexture, in the context of EBSD, refers to the collective orientation of grains within a sample's microstructure. A fundamental example of this is the relationship between individual grain size and orientation. This concept extends to include the misorientation between grains, commonly referred to as macrotexture. With the advancements in EBSD technology, it's now possible to rapidly collect and analyze thousands of orientations per minute, yielding extensive statistical data on various distributions. This capability to correlate texture with microstructure has been instrumental in advancing our understanding of key physical processes, such as recrystallization, grain boundary structure and properties, grain growth, and other critical phenomena. These developments in EBSD techniques have significantly contributed to the fields of materials science and engineering, offering deeper insights into the microstructural characteristics of materials.

Traditionally, identifying phases within the SEM involved inferring phase identity based on phase composition. However, this approach is subject to inherent inaccuracies in quantitative analysis with EDS or WDS in the SEM. Furthermore, this method is less applicable when distinguishing phases with multiple crystal structures but a single

composition, such as TiO_2, which possesses three different crystal structures. Another significant challenge arises in distinguishing austenite from ferrite in engineering steels, as both phases may exhibit very similar chemistries despite differing crystal structures. Enhanced EBSD resolution has been achieved using thin samples that permit electron transmission and diffraction at SEM-accelerated voltages (20–30 kV). Patterns generated in this manner share similarities with EBSD patterns but are formed under transmission conditions, resulting in significantly improved spatial resolution compared to EBSD on bulk samples. Transmission Kikuchi diffraction (TKD) enables the study of macrotexture in ultrafine-grained crystalline materials [15].

To optimize the use of EBSD, a fundamental understanding of crystallography and its representation is invaluable. Numerous excellent books on this subject are available [15,92]. This module will initially clarify the origin of EBSD patterns in the SEM. Subsequently, it will delve into the detectors or cameras used to capture EBSD patterns. Given the critical role of sample preparation in successful EBSD investigations, understanding the methods for producing high-quality samples is crucial. Finally, the module will provide a detailed examination of the experiment itself and its resulting output.

Chapter 3: Materials information and material preparation

3.1 Material selection

Traditional alloys typically have a composition that includes a few main elements and several sub-elements, with limited diversity in types. In contrast, high-entropy alloys (HEAs) are composed of multiple principal elements, each present in equal or nearly equal atomic ratios. This unique composition distinguishes HEAs from conventional alloys.

HEAs are known for their ability to exhibit a single crystal structure. Numerous experiments have demonstrated that they can form either a single body-centered cubic (BCC) or face-centered cubic (FCC) structure phase. Additionally, they can exhibit a mixed-phase structure that combines both BCC and FCC phases. This phenomenon suggests that in HEAs, elements with comparable atomic ratios can solidly dissolve into a simple structure, preventing the formation of complex intermetallic compounds.

The structural characteristics of high-entropy alloys include a simplified microstructure, a reduced tendency to form intermetallic compounds, nanoprecipitation, and the potential for an amorphous structure. These features contribute to their remarkable properties, such as high strength, hardness, resistance to temper softening, and wear resistance.

Various methods, including eutectic and peritectic processes, are utilized to refine the grain size in HEAs [100]. Furthermore, the fine-grain dispersion of a second phase in high-entropy alloys can be effectively used to inhibit grain growth. This aspect is particularly advantageous in the development of eutectic dual-phase high-entropy alloys, an area of active research interest [101].

The key properties and characteristics of high-entropy alloys are summarized in the table below, providing a comparative overview of their distinct features and advantages

over traditional alloy compositions. This summary offers a concise yet comprehensive understanding of the unique attributes and potential applications of HEAs in various fields.

Based on the distinctive alloy characteristics, it becomes evident that eutectic high-entropy alloys exhibit exceptional performance. The properties of many high entropy alloys are shown in Table 3-1. In the case of dual-phase alloys, they are exclusively present in the form of FCC and BCC. As of now, the manufacturing process for multi-component High-Entropy Alloy (HEA) materials often involves conventional methods such as induction melting or vacuum arc melting. This is typically followed by casting and subsequent cycles of remelting. These repeated remelting steps are crucial to ensure the homogeneity and uniform distribution of elemental materials throughout the alloy. However, 3D printing technology offers an alternative approach. It is characterized by rapid heating, cooling, and continuous circulation, which promotes uniformity in the structure and composition of high-entropy alloy components. This effectively addresses the limitations of traditional high-entropy alloys, which tend to have coarse crystal structures, susceptibility to porosity, and compositional segregation. Furthermore, 3D printing significantly accelerates the development and response time for new products.

Table 3-1. Common mechanical properties of high-entropy alloys (Tensile test)

Composition	Phases	Yield Strength $\sigma_{0.2}$	Tensile strength (UTS)	Ductility (ε)
$AlCoCrFeNi_{2.1}$ [100]	FCC+BCC	356Mpa	719Mpa	27%
$FeCrNi_{2.2}Al_{0.8}$ [102]	FCC+B2	479Mpa	956Mpa	12%
$Al_{12.9}Co_{20.9}Cr_{27.3}Fe_{23.9}Ni_{14.9}$ [103]	FCC+BCC	618Mpa	1031Mpa	5%
$Al_{0.25}FeMnNiCrCu_{0.5}$ [104]	FCC+BCC	636Mpa	1052Mpa	24.5%
$Al_{0.7}CoCrFeNi$ [105]	FCC+BCC	771Mpa	1171Mpa	11%
$Al_{19}Fe_{20}Co_{20}Ni_{41}$ [106]	$L1_2$+B2	570Mpa	1060Mpa	50%
$Fe_{49.5}Mn_{30}Co_{10}Cr_{10}C_{0.2}Ti_{0.1}V_{0.1}Mo_{0.1}$ [107]	σ-phase, Cr-rich MC-type carbides, nano-scale (Ti, V, Mo)C	699Mpa	1041Mpa	45%

Nonetheless, the 3D printing process introduces some challenges. The continuous heating cycle leads to variations in the thermal conditions of each layer, resulting in different microstructures in each layer. These microstructural differences consequently affect the mechanical properties. To address this, a thorough analysis of the microstructure of 3D printed materials is conducted, along with tensile experiments on the samples. This enables the establishment of a correlation between microstructure and mechanical properties, contributing to a better understanding of the material's mechanical behavior.

Various dual-phase high-entropy alloys exhibit remarkable properties, prompting extensive research into the application of high-entropy alloys. Notably, $AlCoCrFeNi_{2.1}$ has garnered significant attention due to its outstanding characteristics, as thoroughly explored in the work of Professor Lu [94,97]. The study has delved into the microstructural origin [74,108,109,110] of grain size [102,111−114], high strength, and high ductility within this alloy. This ongoing research has rapidly brought $AlCoCrFeNi_{2.1}$ into the spotlight, piquing interest in the broader application of high-entropy alloys [115].

Subsequently, another high-entropy alloy, incorporating various elements, achieved a significant breakthrough in terms of strength and ductility. Peijian Shi and his team [116] successfully produced high-entropy alloys with exceptional properties using directional solidification techniques, primarily based on the $Al_{19}Fe_{20}Co_{20}Ni_{41}$ alloy. This material boasts an elongation rate of approximately 50% at room temperature and a strength of about 1060MPa. This advancement represents a notable milestone in enhancing the performance of high-entropy alloys. To further understand the influence of the unique microstructure formed via directional solidification on the material's performance, Peijian Shi and his colleagues conducted in-depth investigations. The figure displays the distinctive lamellar structure generated during directional solidification, providing insights into the remarkable ductility and strength achieved by $Al_{19}Fe_{20}Co_{20}Ni_{41}$. This material holds significant research value due to its exceptional properties. A comparison of the mechanical properties of the $Al_{19}Fe_{20}Co_{20}Ni_{41}$ eutectic alloy with other materials can be seen in the accompanying fig 3-1.

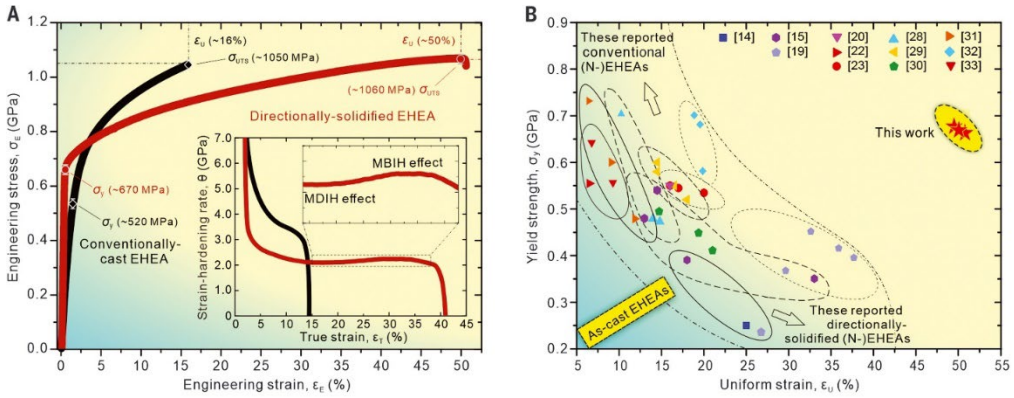

Fig 3-1. Tensile response at ambient temperature [72].

Fig 3-1(A) is engineering stress–strain curves of the directionally solidified EHEA compared with the conventionally cast EHEA, displaying a substantial increase in uniform tensile ductility without any strength reduction. The directionally solidified EHEA shows no post-uniform ductility, which is also confirmed by the absence of macroscopic necking at the fracture end in the inset of fig. S5A. Tensile loading was performed along the DS direction. Inset shows the corresponding strain-hardening

curves. MDIH and MBIH refer to multi-slip dislocation–induced hardening and microband-induced hardening, respectively; ε_U, uniform strain; σ_y, yield strength; σ_{UTS}, ultimate tensile strength. Fig 3-1(B) is yield strength versus uniform strain of the directionally solidified EHEAs compared with those of previously reported as-cast eutectic and near-eutectic HEAs [117−128]. (N-)EHEAs refers to eutectic and near-eutectic HEAs. The conventional (N-)EHEAs include directly cast and arc-melting eutectic and near-eutectic HEAs [129].

As shown in the fig 3-1, the strength and ductility of the material are in the absolute leading position. So, choose this material as the project material. Table 3-2 also shows the crystallographic information of the samples.

Table 3-2. crystallographic information of $Al_{19}Fe_{20}Co_{20}Ni_{41}$

	a	b	c
FCC (L_{12})	5.750	5.750	5.750
BCC (B2)	3.608	3.608	3.608

3.2 Sample preparation

The high purity (99 wt.%) elemental powders of Al, Co, Fe and Ni with spherical morphologies and similar sizes of approximately 150-180 μm diameters (80-100 mesh) were physically mixed in a ball miller according to the nominal composition. The mixing time is 2 hours. The specific printing parameters are shown in the table 3-3 below.

Table 3-3. Fabricating parameters

Process parameters	Details
Deposition current	140 A
Deposition voltage	13.5 V
Traveling speed	50 mm/min
Torch shielding gas flow rate	10 L/min
Shielding cover gas flow rate	25 L/min
Distance of electrode to powder bed	3.5 mm

There are also specific reasons for the parameters in the 3D printing process. The deposition current of 140V and the electrode-to-powder bed distance of 3.5 mm are suitable for promoting stable deposition of powder materials and minimizing splashing. The travel speed of 50 mm/min is suitable to provide sufficient heat input to ensure complete melting of the powder during deposition. The torch shielding gas flow rate of 10 L/min is to minimize oxidation during PAAM processing without blowing the powder away from the powder bed. A shield gas flow of 25 L/min was used to protect the deposited layer from oxidation during the cooling phase.

3.3 Experimental procedure for XRD

The samples were securely positioned on a stand to maintain a level surface. The accompanying fig 3-3 illustrates the schematic diagram of the bracket installation. The bracket itself is a flat metal cylinder featuring a central groove, as depicted by the black segment in the diagram. To affix the sample (shown in gray), a specialized setting glue (indicated in blue) was applied within the groove. Subsequently, a leveling board was used to carefully adjust the sample's position to align perfectly with the surface of the holder. This meticulous process ensured the maintenance of a level sample surface. The materials required to make XRD samples are shown in Fig 3-4. The prepared sample is shown in Fig 3-5.

Following the installation, the holder was inserted into the machine, and X-ray

diffraction (XRD) measurements were conducted using a PANalytical XPert Powder Diffractometer. This instrument was equipped with a Cu target (with Kα1 radiation at 1.54 Å), operated at a voltage of 40 kV, a current of 30 mA, and a scan speed of 0.04 degrees per second. The XRD analysis covered a 2θ range from 30 to 130°.

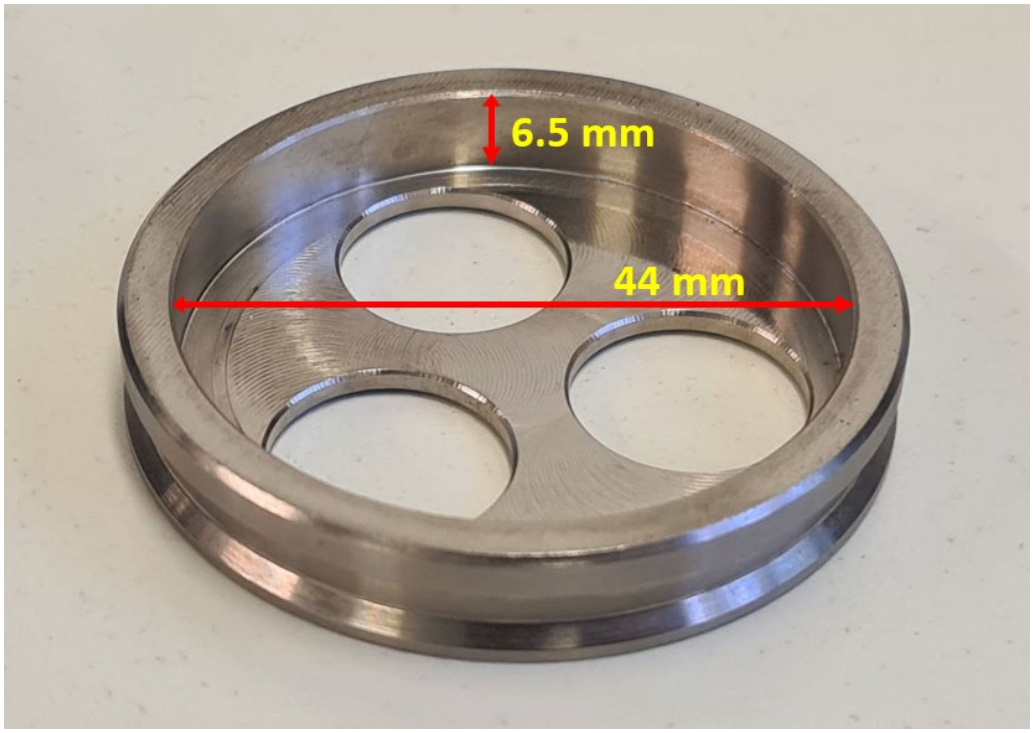

Fig 3-3. Irregular sample holder

Fig 3-4. Items required for XRD instrument sample preparation.

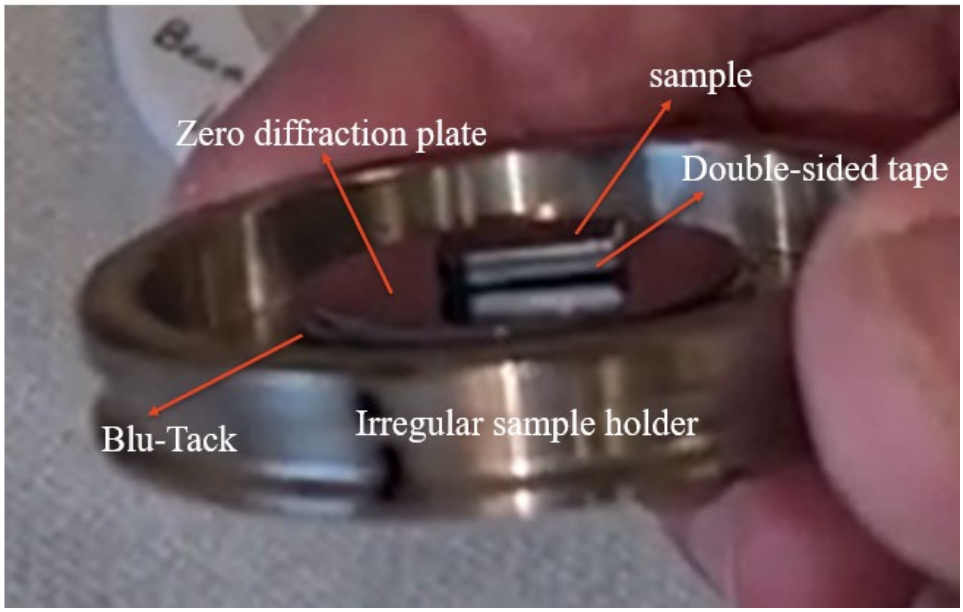

Fig 3-5. Loading flat plate samples

3.4 Experimental procedure for SEM

Samples prepared for SEM analysis underwent a meticulous polishing process involving successive steps. Initially, mechanical polishing was carried out using 1,200 and 4,000 grit sandpaper to achieve a smooth, even surface. Subsequently, oxide polishing suspension (op-s) was employed to further enhance the flatness of the sample. For samples subjected to EBSD and EDS testing, the same procedure was followed, involving mechanical polishing with 1,200 and 4,000 grit sandpaper and the use of oxide polishing suspension (op-s) to attain a flat surface.

To achieve an impeccably flat and clean sample surface, argon ion milling was performed in the Gatan Precision Etch Coating System (PECS) II. This milling process involved grinding at 1 kV for 15 minutes at a temperature of -50 °C. These steps collectively ensured the optimal preparation of samples for analysis. The prepared samples are shown in Fig 3-2.

When conducting experiments with EBSD, step size is 0.25μm.

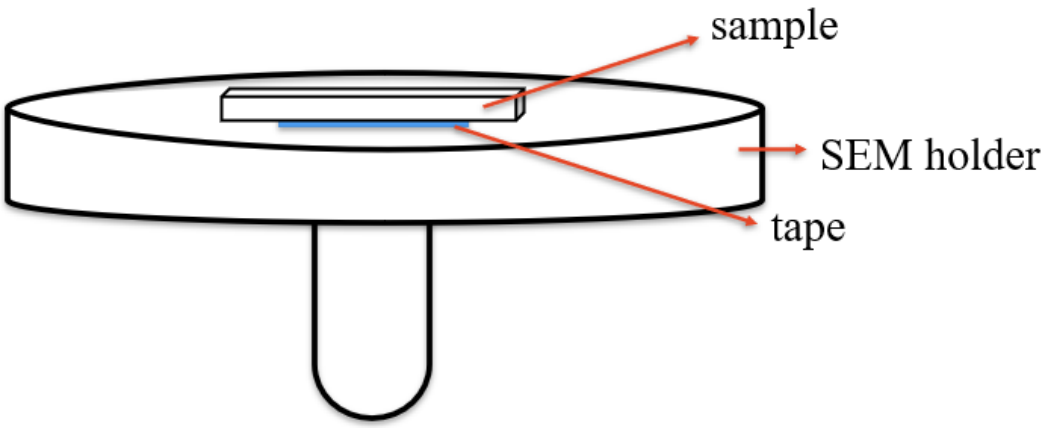

Fig 3-2. Schematic of SEM sample.

3.5 Experimental procedure of tensile test

The samples designated for hardness testing underwent a preparation process involving mechanical polishing. This preparation included the use of 1,200 and 4,000 grit sandpaper, to achieve a flat and smooth surface.

3.6 Experimental procedure of hardness test

The samples designated for hardness testing underwent a preparation process involving mechanical polishing. This preparation included the use of 1,200 and 4,000 grit sandpaper, followed by oxide polishing suspension (op-s) application, to achieve a flat and smooth surface. The hardness of these materials was determined using the Vickers hardness test method.

In this test, a standard square pyramidal diamond indenter, exerting a force of 1 kilogram, was pressed into the surface of the sample. The test force was maintained for a specified duration, after which the force was removed, and the length of the resulting root diagonal on the sample surface was measured. Subsequently, the hardness value was calculated by referencing the appropriate table or standard.

The specific instruments and experimental parameters for hardness testing are shown in Table 3-4.

Table 3-4. Vickers hardness measurements specific information

The brand of hardness tester	Shimadzu Type M 73087
Load	1000g
Duration	30s
Number of measurements	1

Chapter 4: Results

4.1 XRD

We conducted tensile tests on the stretched samples by cutting and stretching them in different areas and conducted XRD detection. We took 2-4mm, 4-6mm, 6-8.5mm and 8.5-11mm from the top for experiments. Electron diffraction conducted by another student in our group confirmed the existence of $L1_2$ and B2 phases, not the simple FCC and BCC. I compared the data of each sample to the standard card and found that the stretched sample is still in the $L1_2$ and B2 phases, and there is no third phase. Therefore, no phase change occurred during the entire tensile experiment. The specific XRD data is shown in Fig 4-1.

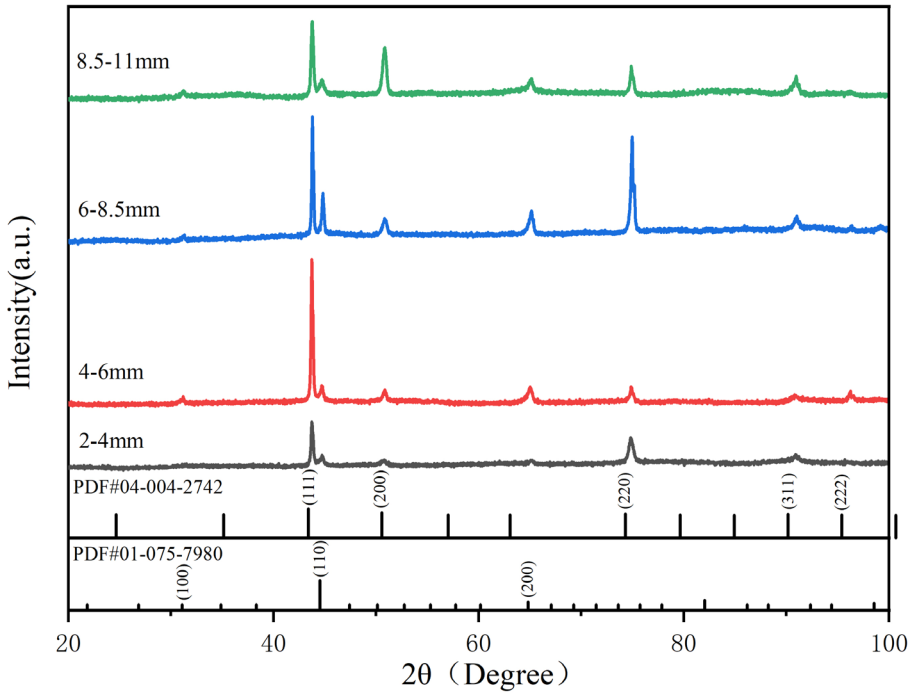

	a	Crystal structure
PDF#04-004-2742	3.608	FCC ($L1_2$)
PDF#01-075-7980	5.750	BCC(B2)

Fig 4-1. XRD data of each layer of samples from the top

4.2 EBSD

Since the material is obtained using 3D printing, the top, middle and lower structures of the material form microstructures with different morphologies due to the influence of thermal cycles. Therefore, as shown in Fig 4-2, the locations 3mm, 13mm and 9mm from the top were selected for analysis. The first is the top position. Fig 4-2 (a, b, c) shows the top electron backscattered diffraction (EBSD) phase diagram and inverse polar figure, indicating that the EHEA at the top of the 3D printing material has a typical co-existing eutectic microstructure of Lamellar and Grid. Adjacent grains have different growth directions. Among the grains at the top, $L1_2$ and B2 have fixed orientation relationships and most of them follow the K-S orientation relationship. The reason why the two phases do not strictly follow the K-S parallel relationship is because of the angular offset. The angle shift is caused by thermal cycling. But I also discovered new orientation relationships of special grains (see Fig 4-5 (a, b)). In addition, as can be seen from Fig 4-3 (a), the corresponding contents are $L1_2$~72.3 vol.% and B2~27.7 vol.% respectively. Fig 4-6 (a, b) is the electron backscattered diffraction (EBSD) phase diagram and inverse polar figure of the middle top. In the process from the top to the middle, the Grid gradually becomes smaller until it disappears. In the middle, it is shown that the 3D printed EHEA has a typical Lamellar-like eutectic microstructure. This morphology is also the most common microstructure of this material. Moreover, in the middle part, the orientation relationship of the two phases follows the K-S orientation relationship (Fig 4-7). Furthermore, as can be seen from Fig 4-7, the average thicknesses of B2-coarse (blue) lamellae and $L1_2$-fine (red) lamellae are ~2.3 and 1.59 μm, respectively, and the corresponding contents are divided into ~47.5 vol. % and 52.5 vol.%. Fig 4-8 (a, b) shows the microstructure of the material at the bottom. At the bottom, the grid-like microstructure reappears. But unlike the top, the Grid phase at the top is the B2 phase wrapping the $L1_2$ phase. At the bottom, the $L1_2$ phase wraps the B2 phase. At the bottom, it was also found that $L1_2$ and B2 both followed the K-S orientation relationship, and no new orientation relationship was found [130]. The phase content changes of $L1_2$ and B2 are ~38.5 vol.% and 61.5 vol.%. These results indicate

that from the top to the bottom, the $L1_2$ content gradually decreases while the B2 content gradually increases. The reason for the obvious change in phase content is that the Al content changes very obviously during the printing process. Furthermore, all EBSD phase diagrams confirm that the existing phases are L_{12} and B2 phases respectively. This conclusion can also be confirmed in the XRD pattern.

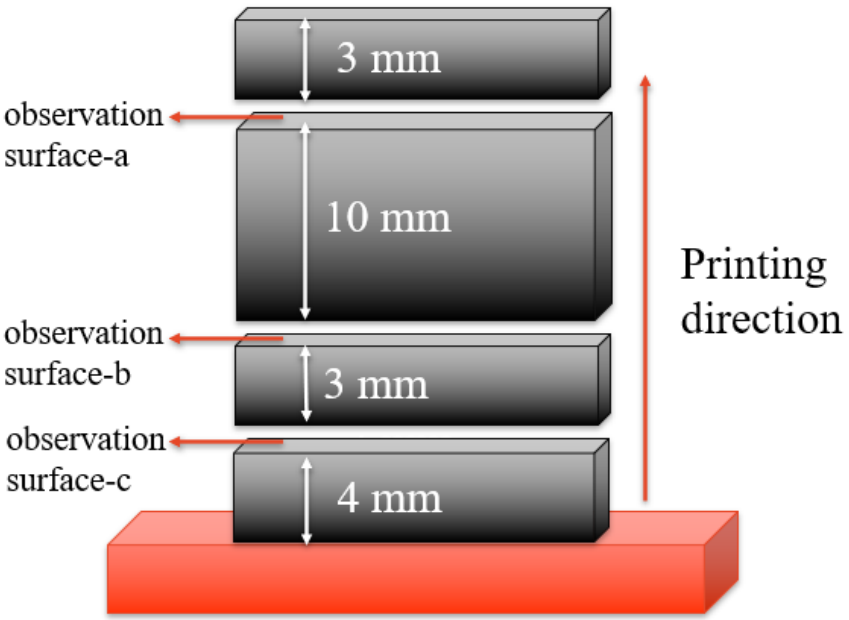

Fig 4-2. Sample sampling location: (a) Top sample collection location and information; (b) Middle sample collection locations and information; (c) Bottom sample collection location and information.

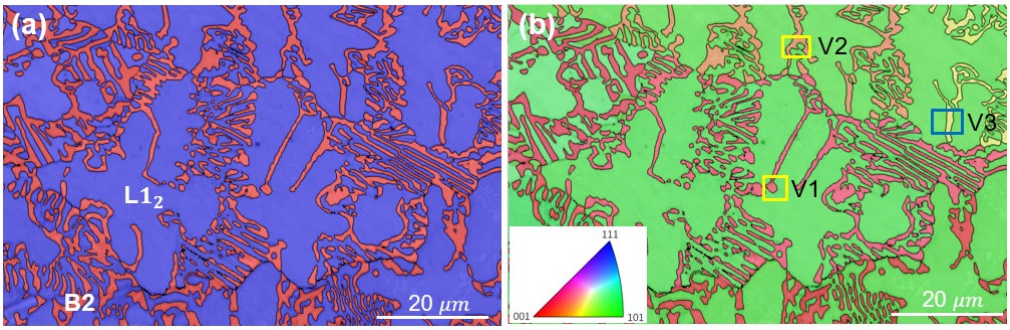

Fig 4-3. Microstructure of the top of the 3D printing sample: (a) EBSD phase map; (b) inverse pole figure.

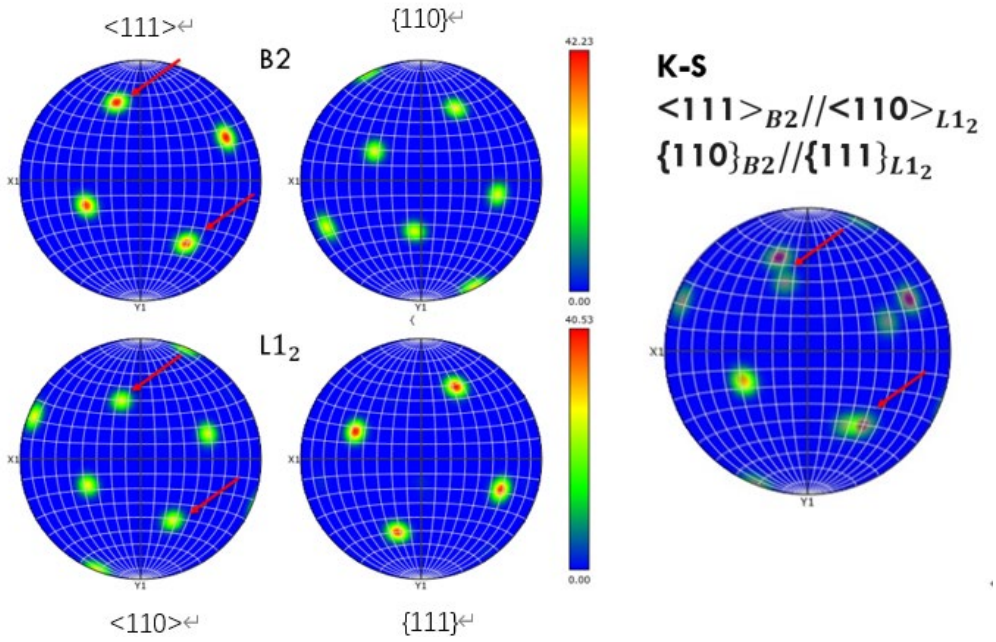

Fig 4-4. V1 and V2 areas: Microstructure of the top of the 3D printing sample: (a) EBSD phase map; (b) inverse pole figure.

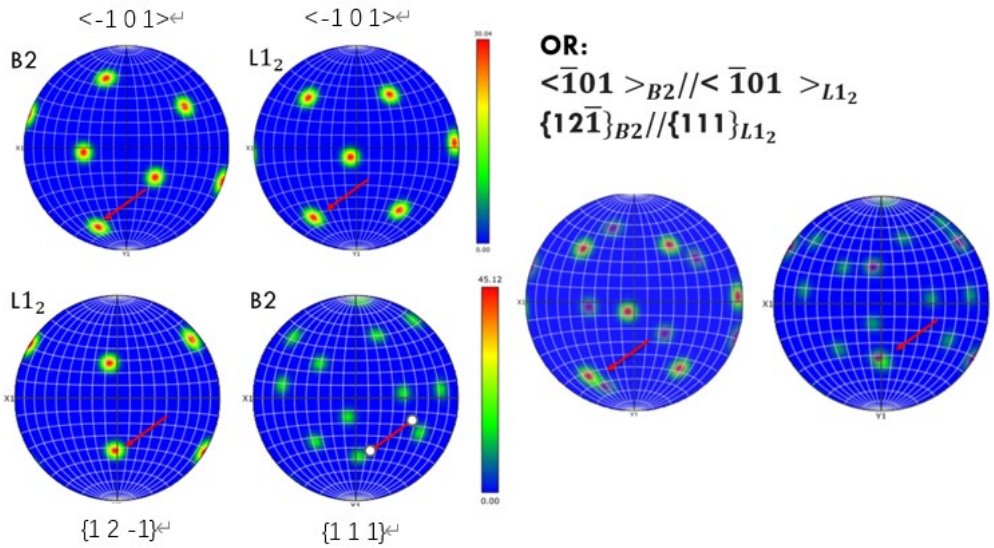

Fig 4-5. V3 areas: Microstructure of the top of the 3D printing sample: (a) EBSD phase map; (b) inverse pole figure.

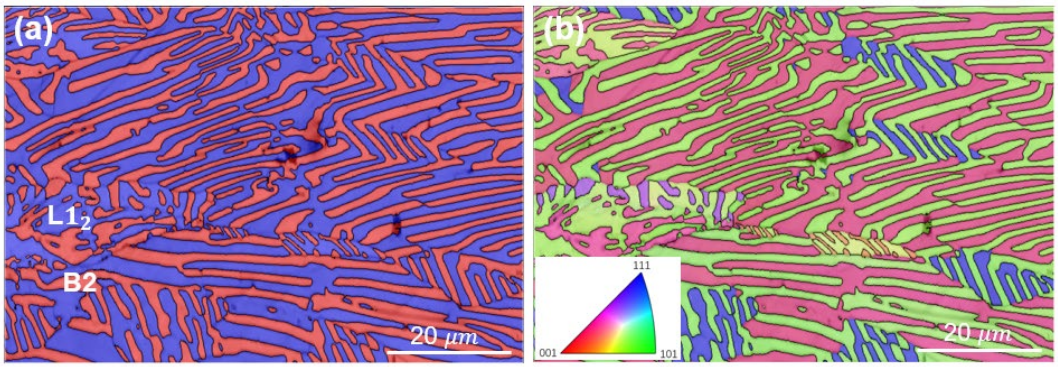

Fig 4-6. Microstructure of the middle of the 3D printing sample: (a) EBSD phase map; (b) inverse pole figure

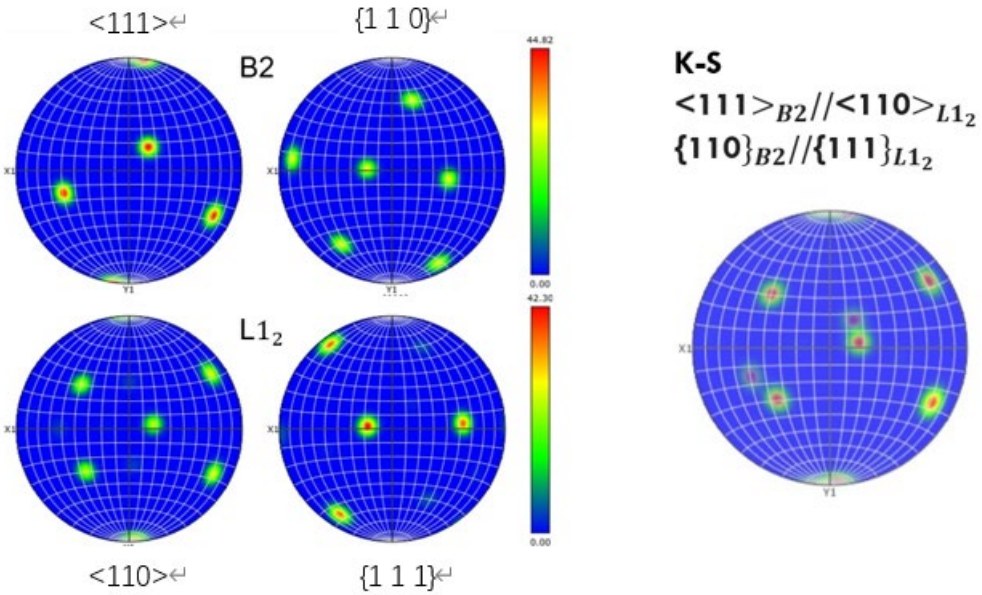

Fig 4-7. Microstructure of the middle of the 3D printing sample: (a) EBSD phase map; (b) inverse pole figure.

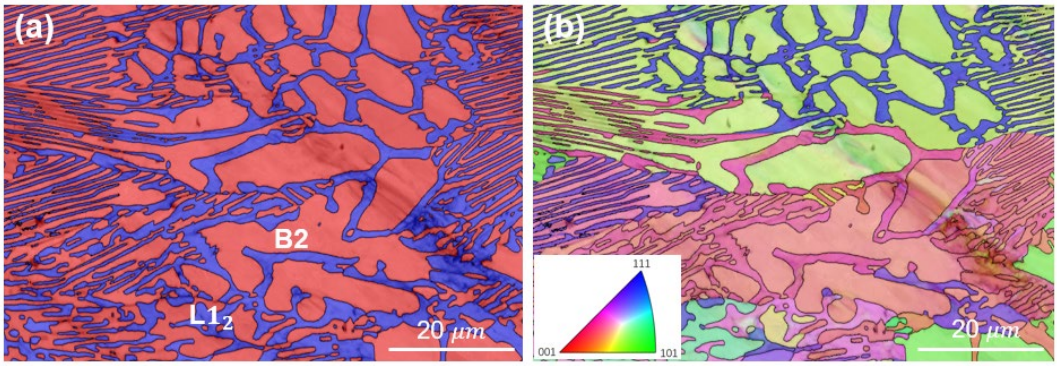

Fig 4-8. Microstructure of the bottom of the 3D printing sample: (a) EBSD phase map; (b) inverse pole figure ;

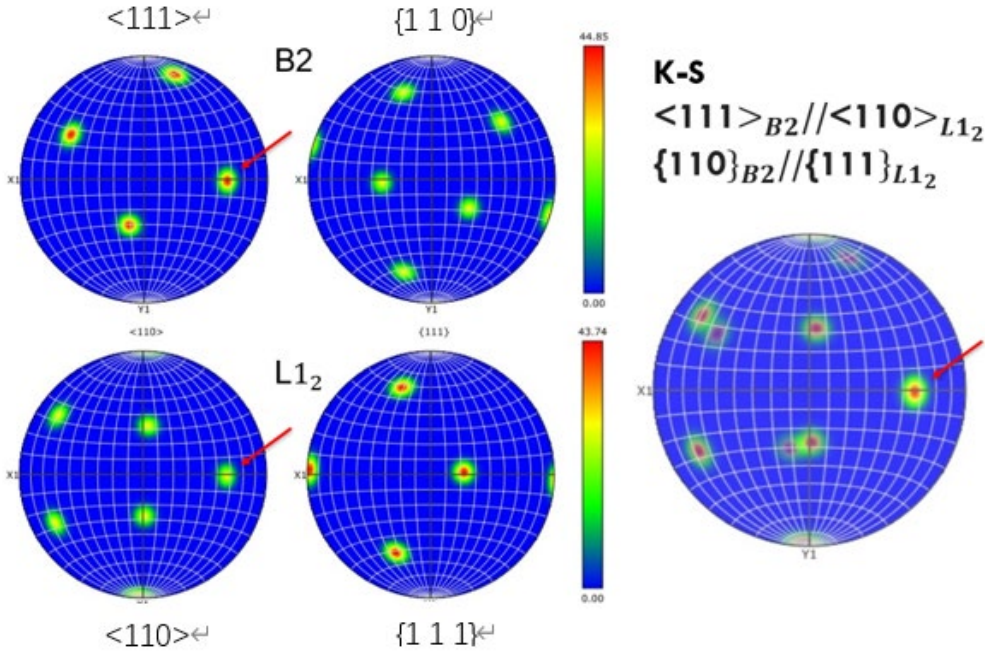

Fig 4-9. Microstructure of the bottom of the 3D printing sample: (a) EBSD phase map; (b) inverse pole figure.

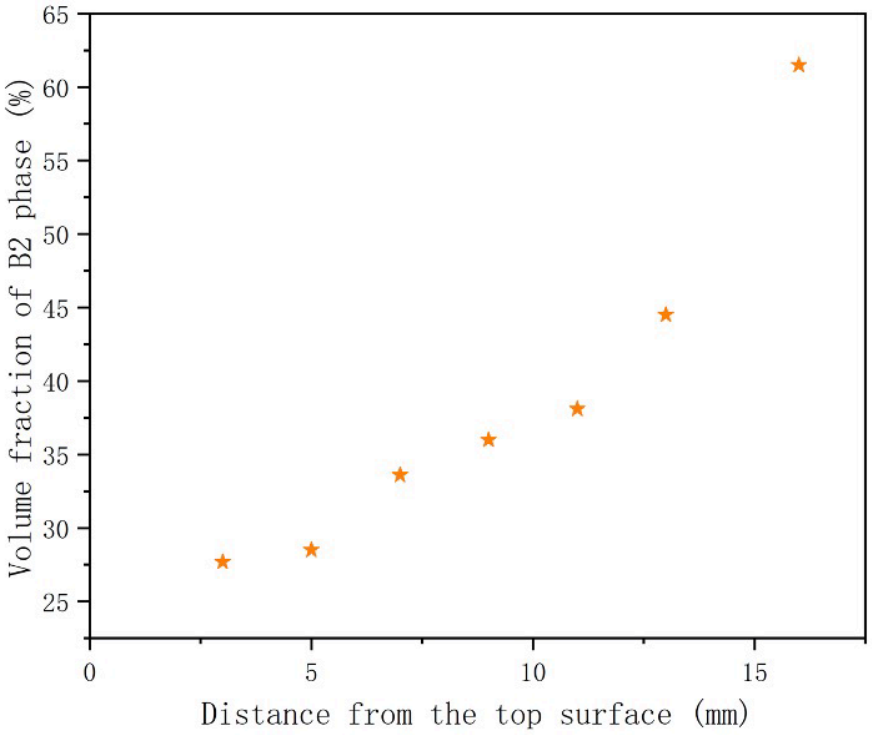

Fig 4-10. Sample B2 phase content

Table 4-1. B2 content in the sample

Distance from the top surface (mm)	Volume fraction of B2 phase (%)
3	27.7
5	28.5
7	33.6
9	36
11	38.1
13	47.5
16	61.5

As the number of printed layers increases, the bottom experiences the most cyclic thermal loading with the build direction. The phase content changes. The position closer to the bottom has more BCC phases. The specific changes are shown in Fig 4-10, and the detailed contents are presented in Table 4-1.

4.3 EDS

We use SEM-EDS for elemental analysis of materials. Fig 4-11 and Table 4-2 shows the energy dispersive X-ray spectroscopy (EDS) diagrams of individual elements of Al, Co, Fe, and Ni in EHEA during the 3D printing process. The EDS pattern shows that the B2 phase is poor in Co and Fe but enriched in Ni and Al, and the $L1_2$ phase is only depleted of Al. The error bar that appears in the table is the maximum and minimum value of the element content within a fixed range of the elements in the table. It can be seen from the table that there are very obvious changes in the aluminum element in the upper, middle and lower parts of the material. The Al element continues to decrease from the bottom to the top, and this decrease in Al element leads to different phase contents. The variation of Al content along the build direction is discussed from four perspectives.

(1) Powder Reuse

Reuse of the powder in the manufacturing process will result in lower content, but not as much. The content loss is about 1%.

(2) Al has a higher vapor pressure

Al will preferentially evaporate from the molten pool. If this phenomenon occurs, the Al content should be lower than the set content during the entire printing process, rather than showing a decreasing trend from bottom to top.

(3) Al element splash

The sputtering phenomenon of Al will produce Al-based oxides on the surface of the material, but our elemental analysis of the sample did not detect the presence of a large amount of oxides.

(4) Overheating input and poor air protection during printing

This situation results in a loss of all elements, not just the Al element. And there will not be a very obvious trend in the top, middle and bottom directions.

Table 4-2. The content of elements in each phase (wt %)

		phase	Al	Fe	Co	Ni	C
TOP	Lamellar	$L1_2$	6.5±0.1	23.4±0.1	23.1±0.1	44.7±0.2	2.3±0.2
		B2	10.3±0.1	20.4±0.1	21.1±0.1	45.7±0.2	2.5±0.2
	Grid	$L1_2$	6.8±0.1	23.6±0.1	23.5±0.1	42.6±0.2	3.5±0.2
		B2	10.8±0.1	19.6±0.1	20.6±0.1	46.4±0.1	2.6±0.2
	whole		7.5±0.1	22.4±0.1	22.7±0.1	44.2±0.2	3.2±0.2
middle	Lamellar	$L1_2$	6.9±0.1	23.4±0.1	24.4±0.2	42.8±0.2	2.5±0.1
		B2	9.9±0.1	20.5±0.1	24.2±0.2	42.7±0.2	2.7±0.2
	whole		8.7±0.1	21.4±0.1	24.4±0.1	42.5±0.2	3.0±0.2
bottom	Lamellar	$L1_2$	6.5±0.1	23.5±0.2	23.8±0.2	43.8±0.2	2.4±0.2
		B2	9.7±0.1	20.5±0.2	21.7±0.2	45.7±0.2	2.4±0.1
	Grid	$L1_2$	6.7±0.1	24.1±0.1	23.4±0.2	43.3±0.2	2.5±0.2
		B2	10.6±0.1	19.4±0.1	20.3±0.2	47.1±0.2	2.6±0.2
	whole		9.1±0.2	22.1±0.1	22.0±0.1	44.3±0.2	2.5±0.2

Note that significant amount of carbon (> 2.3 wt.%) was detected in all samples, which could be introduced during additive manufacturing process and SEM sample surface contamination.

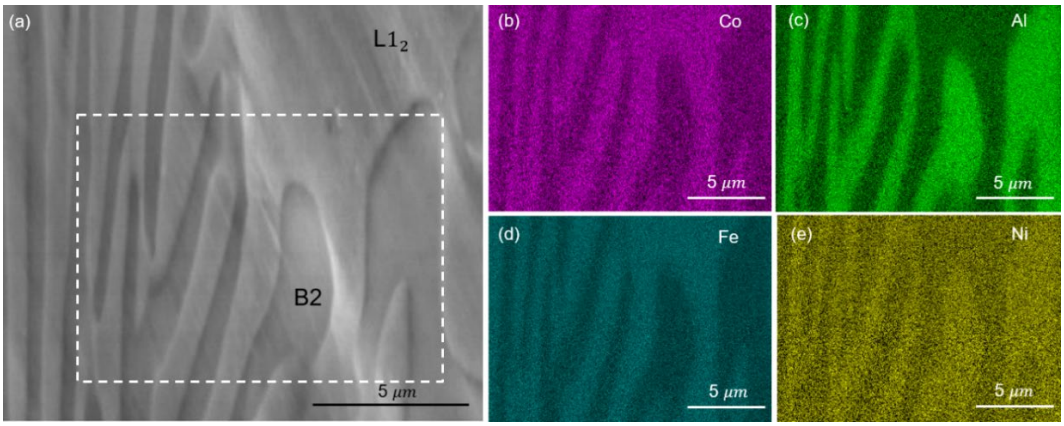

Fig 4-11. $Al_{0.95}CoFeNi_{2.05}$ EDS map

4.4 Tensile test

Mechanical property tests were conducted on various sections of the sample, with the specific printing regions corresponding to those outlined in Table 4-3, and the detailed performance curves are presented in Fig 4-12. Considering the longstanding issue of high porosity encountered by many samples during the 3D printing process, reference data is unnecessary. Only the upper region of the sample1 is deemed suitable for

analysis. In this region, the $L1_2$ phase and B2 phase partially exhibit a layered structure with an alternating arrangement. Additionally, a portion of the $L1_2$ phase experiences expansion, resulting in a grid-like microstructure of the $L1_2$ and B2 phases. The properties of the examples are as shown in Table 4-4.

Table 4-3. The sample serial number corresponds to the sample location.

Sample number	Distance from top surface (mm)
1	**2-4**
2	**4-6**
3	**6-8**
4	**8-10**
5	**10-12**

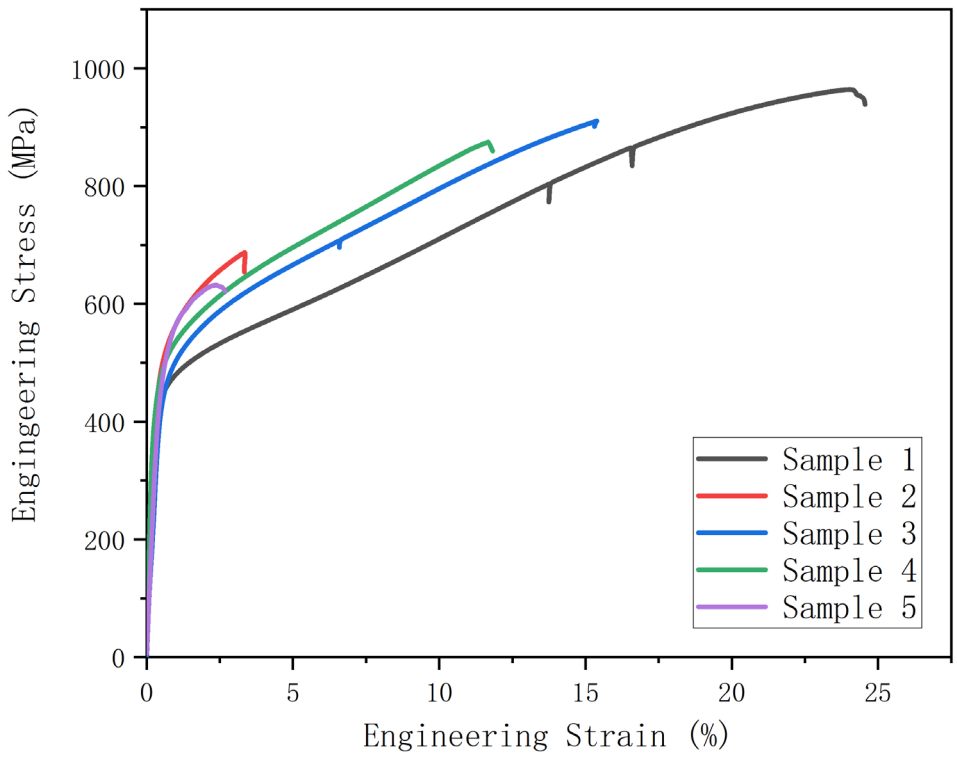

Fig 4-12. Tensile response of the 3D printing $Al_{0.95}CoFeNi_{2.05}$

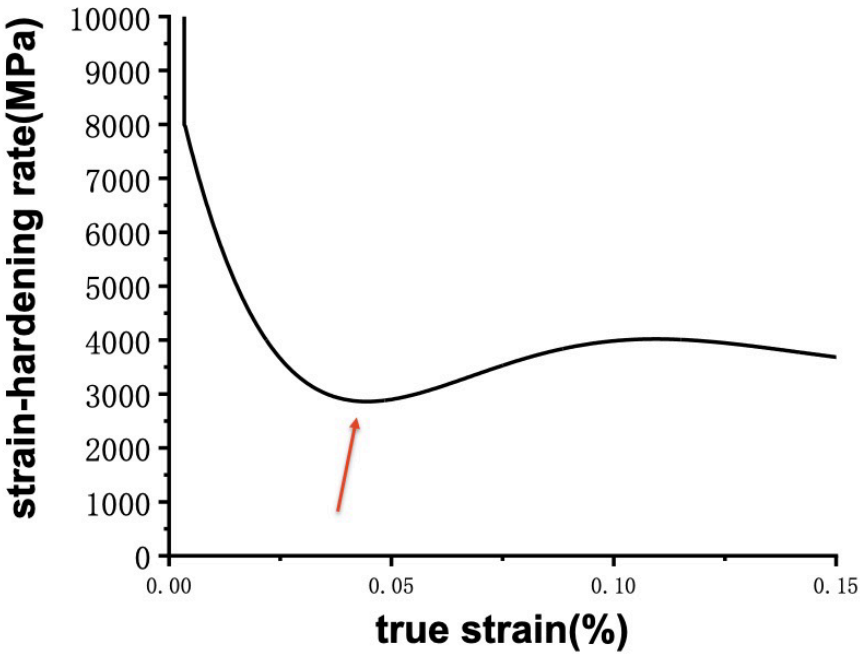

Fig 4-13. Strain-hardening rate of 3D printed high-entropy $Al_{0.95}CoFeNi_{2.05}$ (sample 1)

Table 4-4. The performance value of 3D printed high-entropy alloy is sample 1.

Yield strength (σ_y)	450 MPa
Ultimate strength (σ_{UTS})	960 MPa
Tensile strain (ε_U)	24.5 %

Samples 1-5 represent different compositions, as shown in Table 4-2. $L1_2$ is the soft phase, and B2 is the hard phase. As the content of $L1_2$ decreases from top to bottom and the content of B2 increases, the hardness of the samples increases gradually from the top to the bottom in the printed sample, while ductility decreases gradually. At the same time, the lamellar structure plays a role in enhancing the material's ductility.

Regarding the work hardening rate curve (Fig 4-13), this graph can represent the material's sensitivity to work hardening at different strain states, ranging from 2mm to 4mm. The turning point in the curve occurs because initially, only the $L1_2$ phase deforms. Later, the B2 phase also begins to participate in deformation, causing the curve to rise.

4.5 Hardness

The material's hardness consistently rises with an increase in B2 content, reaching a peak hardness of 585HV (Table 4-5, Table 4-6, Fig 4-14, and Fig 4-15). This is primarily observed in the section of the material located 13mm from the top, where the $L1_2$ and B2 content is nearly evenly distributed at approximately 50% each. The hardness of the material gradually increases as it descends from the top to the 13mm position, primarily due to a higher $L1_2$ content. However, within the section spanning from 13mm to 16mm, there is a rapid increase in the B2 content over a 3mm distance. Consequently, this transition zone results in noticeable hardness fluctuations, particularly at the 13mm level from the top.

Table 4-5. Hardness testing of 3D printed $Al_{0.95}CoFeNi_{2.05}$

Distance from top (mm?)	Average Diagonal Length	Hardness (HV)	Distance from top	Average Diagonal Length	Hardness(HV)
0	57.23	567	5	57.07	569
0.5	57.20	567	5.5	57.02	571
1	57.22	567	6	56.98	571
1.5	57.19	567	6.5	56.03	571
2	57.22	567	7	56.99	571
2.5	57.19	567	7.5	56.95	571
3	57.17	567	8	56.92	573
3.5	57.13	569	8.5	56.94	573
4	57.14	569	9	56.91	573
4.5	57.10	569	9.5	56.87	573
10	56.84	575	15	56.56	579
10.5	56.82	575	15.5	56.52	581
11	56.84	575	16	56.53	581
11.5	56.79	575	16.5	56.44	583
12	56.74	577	17	56.47	581
12.5	56.77	575	17.5	56.41	583
13	56.70	577	18	56.37	583
13.5	56.64	579	18.5	56.33	585
14	56.67	577	19	56.39	583
14.5	56.61	579	19.5	56.29	585
			20	56.73	577

Table 4-6. The standard indentation length of 1kg load corresponds to the hardness value

D	0.0	0.1	0.2	0.3	0.4	0.5	0.6	0.7	0.8	0.9
53	660	658	655	653	650	648	645	643	641	638
54	636	634	631	629	627	624	622	620	617	615
55	613	611	609	606	604	602	600	598	596	593
56	591	589	587	585	583	581	579	577	575	573
57	571	569	567	565	563	561	559	557	555	553
58	551	549	547	546	544	542	540	538	536	534
59	533	531	529	527	526	524	522	520	519	517
60	515	513	512	510	508	507	505	503	502	500

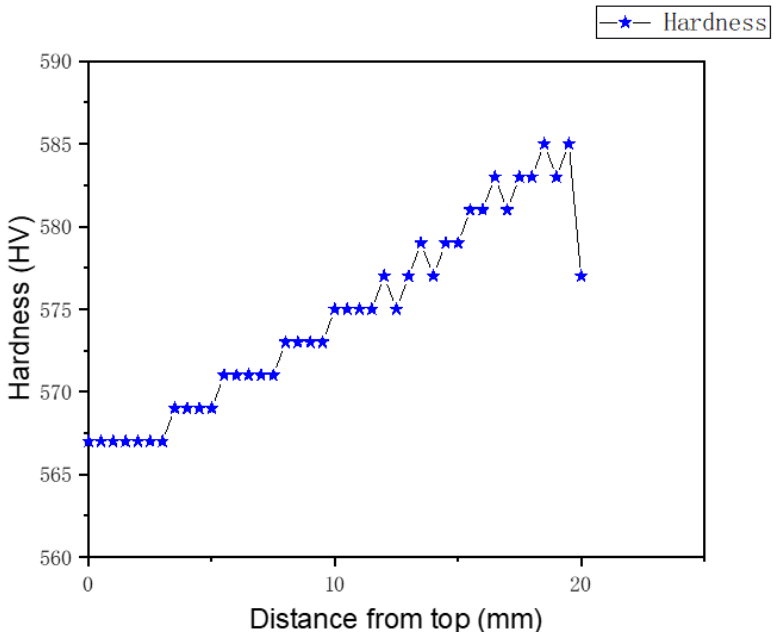

Fig 4-14. Hardness test curve of 3D printed $Al_{0.95}CoFeNi_{2.05}$

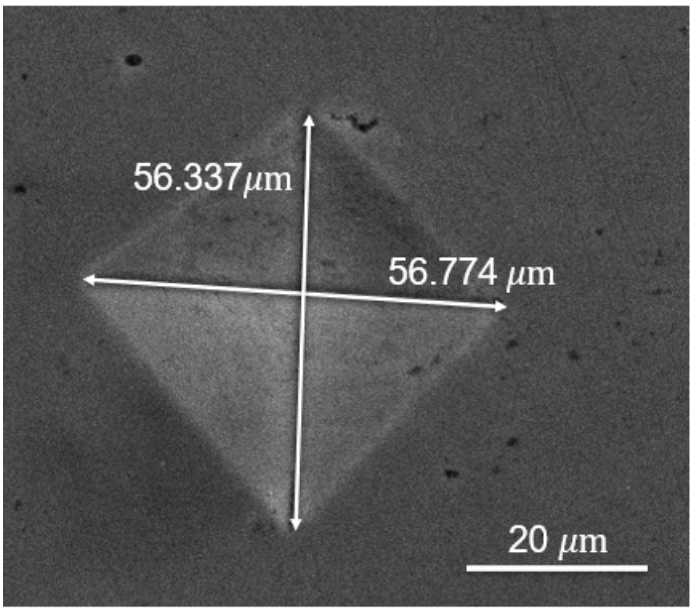

Fig 4-15. Hardness test indentation of 3D printed $Al_{0.95}CoFeNi_{2.05}$

4.6 Fracture Analysis

To gain deeper insights into the apparent strain hardening behavior observed in the $L1_2$ sheets of the developed High-Entropy Alloy (HEA), I conducted an examination of the fracture morphology. Scanning Electron Microscopy (SEM) was employed to scrutinize the microstructure of the fracture surface, revealing a predominant groove-like microstructure. Notably, two distinct fracture modes were identified: ductile fracture of the $L1_2$ phase and brittle fracture of the B2 phase. Given that the $L1_2$ phase is characterized as a soft phase and the B2 phase as a hard phase, our analysis was conducted in conjunction with the work hardening curve.

The inferred mechanism suggests that during tensile deformation, the hard B2 phase experiences minimal deformation, while the soft $L1_2$ phase undergoes stretching. Subsequently, the $L1_2$ phase narrows to form a sharp, bright line without any indentations. This trend ultimately results in the B2 phase undergoing minimal deformation at the bottom of the trench.

These observations are further substantiated in Fig 4-16. It is noteworthy that, despite the anticipated significant stress concentrations around the phase interface due to the

minimal plastic deformation of the B2 phase, no phase interface cracks or debonding were detected on the current fracture surface. This atypical behavior can be attributed to two primary factors: (i) the 3D printed EHEA exhibits a semi-coherent interface combination at the atomic level, offering sufficient resistance to high interfacial shear forces; (ii) the presence of dislocations and multiple dislocations, coupled with secondary slip events, leads to the accumulation around the phase interface. This accumulation contributes to the formation of effective long-range strain gradients, mitigating stress concentrations at the interface. These conclusions are generally supported by the work hardening rates obtained in tensile tests.

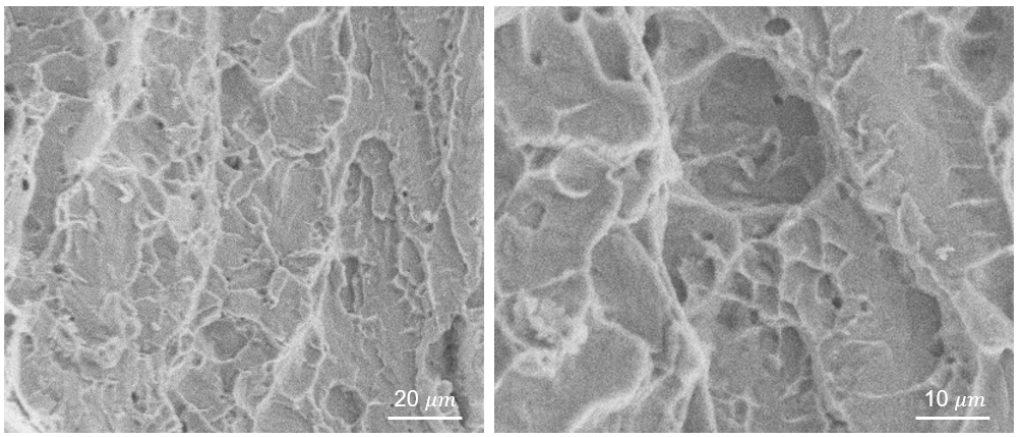

Fig 4-16. Typical SE/BSE-SEM images showing a trench-like fracture morphology featuring the mixed ductile and brittle fracture modes.

Chapter 5: Discussion

This chapter discusses the mechanisms by which materials stretch and some of the subprocesses that occur during deformation.

5.1 Microstructure

As shown in Fig 5-1, lamellar morphology can be seen at all stages of material printing, but only the grid-like morphology appears at the top and bottom ends. However, these grid-like morphologies are composed of different phases. Through the EDS experiment, I can know that the Al element has undergone relatively large and obvious changes from top to bottom of the material (Table 4-2). At the bottom, because the sample is rich in Al elements, the B2 phase rich in Al elements expands and expands to form a grid. At the same time, the proportions of $L1_2$ and B2 are approximately 38.5% and 61.5% respectively. This structural scaling can be seen in the EBSD data, as shown in Fig 5-1. However, the middle part of the sample, that is, the morphological structure of the printed middle section has undergone relatively large changes. Fig 4-6 shows that the middle part of the sample only exhibits a single lamellar structure, and the grid disappears. As the aluminum element gradually decreases from the bottom to the middle, the material reaches the eutectic concentration, forming a eutectic reaction accompanied by the redistribution of atoms to form a layered structure of α and β phases. In the middle part, the contents of $L1_2$ phase and B2 phase also tend to be equal, with $L1_2$ phase and B2 phase being approximately 52.5% and 47.5% respectively. At the top, due to the further reduction in Al content, the B2 content drops significantly. Therefore, the $L1_2$ content increases and expands to form a grid shape. As shown in Fig 4-3, the content changes of $L1_2$ and B2 are approximately 72.3% for $L1_2$ and 27.7% for B2. The continuous decrease of the Al element from the bottom to the top has been a persistent issue with the PAAM technique, and the cause of this problem has not yet been clear. Further research is needed in the future. At the same time, I also found grains at the top of the sample that did not conform to the K-S orientation relationship. At the v3 site at

the top of the sample, I found a new orientation that does not belong to the K-S orientation relationship. As shown in Fig 5-2, $L1_2$ deviates by 5° on [101], while the B2 phase deviates by 4.79° on [102]. How this orientation relationship affects mechanical properties requires further study.

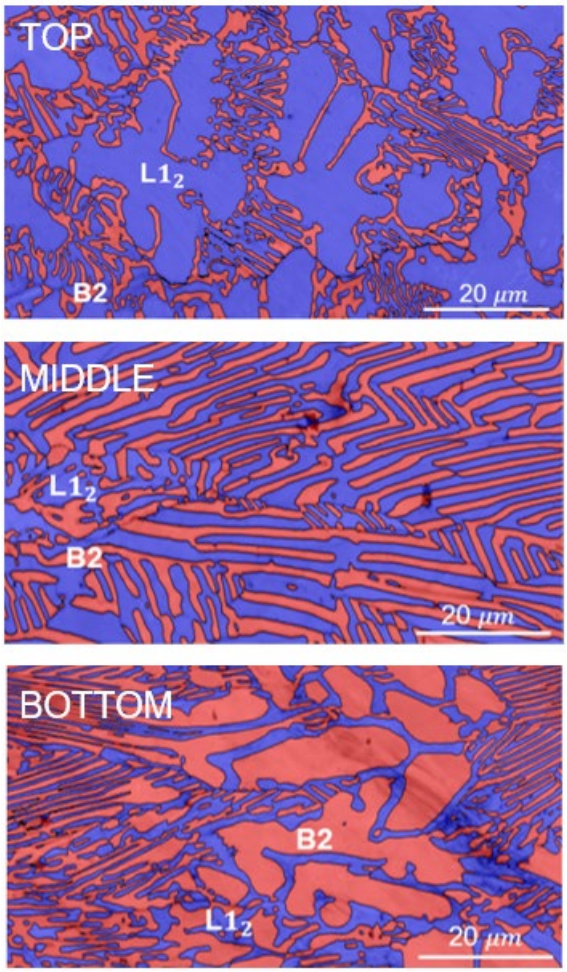

Fig 5-1. Schematic diagram of the microstructure of the top, middle and bottom layers of the sample

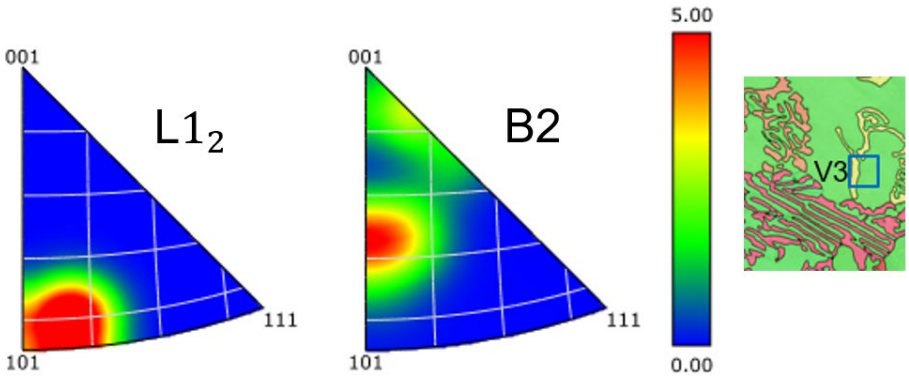

Fig 5-2. Grain orientation relationship at the top V3 site

5.2 Mechanical properties

Table 5-1. Mechanical properties of HEA manufactured by different manufacturing methods.

	Production method	Yield strength (σ_y)	Ultimate tensile strength (σ_{UTS})	Uniform strain (ε_U)
$Al_{0.95}CoFeNi_{2.05}$ **(project sample)**	3D printing-PAAM	450 MPa	960 MPa	24.5%
$Al_{0.95}CoFeNi_{2.05}$	Conventionally cast	520 MPa	1050 MPa	16%
$Al_{0.95}CoFeNi_{2.05}$	Directionally solidified	670 MPa	1060 MPa	50%
$Al_{19.25}Co_{18.86}Fe_{18.36}Ni_{43.53}$	Conventionally cast	486 MPa	956 MPa	10%

As shown in Table 5-1, the mechanical properties of the same materials vary greatly. Therefore, the production method has a great influence on the mechanical properties of the material. Since the 3D printing process is also a directional solidification method, the layered herringbone microstructure that only appears in the directional solidification method also appears in the 3D printed materials. The layered herringbone microstructure significantly improves the ductility of the material. Therefore, materials manufactured using 3D printing will be superior to HEA manufactured traditionally in terms of ductility. Due to the loss of Al elements, grid-like and lamellar shapes coexist

at the top of the sample. At the same time, the top of the material is dominated by the $L1_2$ phase, so the strength of samples produced by 3D printing is lower than that of samples produced by traditional manufacturing and directional solidification. The performance of HEA made of the same elements in different proportions is far inferior to the strength and ductility of the $Al_{0.95}CoFeNi_{2.05}$ alloy.

Since 3D printing technology is also a method of directional solidification, it exhibits the unique herringbone microstructure that is characteristic of directional solidification methods. The herringbone microstructure can improve the ductility within the material, which is why Sample 1 possesses higher ductility than cast alloys. Due to the higher content of $L1_2$ phase in Sample 1, which is a softer phase that swells and increases in size due to the decline in Al content, the grain size becomes larger. As a result, the strength of Sample 1, when compared to cast alloys, is lower.

5.3 Relationship between microstructure and mechanical properties

The emergence of a grid-like microstructure is attributed to the reduction in Al content, which leads to an increase in the $L1_2$ phase and causes expansion. The effect of this grid-like appearance on the mechanical properties of the material requires further investigation. However, the presence of this grid pattern increases the grain size of the material, and an increase in grain size can lead to a decrease in mechanical performance. Sample 1 demonstrates exceptional ductility and features a herringbone microstructure. Therefore, the excellent mechanical properties of Sample 1 are closely related to its herringbone microstructure. Hence, our analysis mainly focuses on the impact of the herringbone structure on the material's mechanical properties.

Herringbone microstructure will significantly increase the ductility of the material. As the $L1_2$ phase expands to form a grid, the content of the herringbone microstructure phase decreases, resulting in a decrease in the ductility of the material.

The good mechanical properties of sample 1 are mainly attributed to the formation of a two-phase layered structure through the eutectic reaction within the material and the layered herringbone structure produced by the directional solidification method (Fig 5-3). The excellent properties of many high-entropy alloys that undergo eutectic reactions are usually attributed not only to the fine layered composite microstructure and high phase interface density, but also to the coordinated co-deformation of alternating hard and ductile phases [8,14,15]. The formation of the microstructure of the layered herringbone structure can significantly improve the ductility of the material. In the directionally solidified layered herringbone structure, microcracks occurring in the B2 phase are impeded at the interface of alternating adjacent $L1_2$ lamellae in region a. These softer $L1_2$ sheets serve as crack buffers, acting on the tips of microcracks to blunt them and shield the associated high local stresses [70,131,132]. Without this alternating soft buffer, cracks would propagate further. When a microcrack traverses the entire B2 lamella cross-section, the adjacent soft L_{12} lamellae blunt the crack tip (Fig. 4-12).

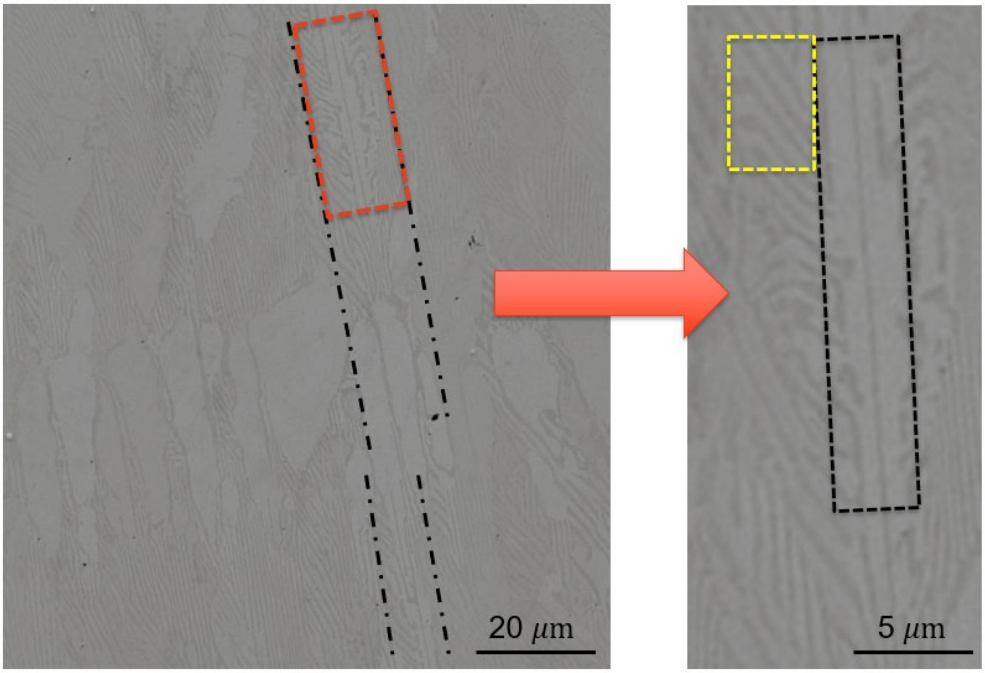

Fig 5-3. The directionally solidified EHEA with a hierarchical herringbone microstructure.

In the context of fracture initiation in the described material, a microcrack must navigate through the $L1_2$ lamellae, encompassing the entirety of region a, and then extend into the neighboring region b. This requirement highlights a dual-level crack arrest characteristic inherent in the herringbone microstructure of the directionally solidified eutectic high-entropy alloy (EHEA). The first level of crack arrest is provided by the alternating hard and soft phase layers of B2 and $L1_2$. The second level is due to the varying arrangement of eutectic clusters within the structure. This complex arrangement imparts the EHEA with exceptional fracture toughness [133].

Another noteworthy aspect of this material's behavior under stress is observed during stretching. New microcracks often initiate in the intact material areas between the already fully extended cracks within each B2 flake. This phenomenon, referred to as the refinement of the crack pattern, plays a crucial role in reducing stress concentrations around the phase interface. It also effectively reduces the stress intensity at the tips of larger microcracks, as detailed in references [134−139].

The ability of the herringbone EHEA to distribute and mitigate stress in this manner underlines its potential for applications where materials are required to withstand high stress or fracture scenarios. The material's structure, characterized by its unique herringbone microstructure and the strategic arrangement of its constituent phases, provides a blueprint for the development of high-performance materials with enhanced toughness and durability.

Chapter 6: Conclusions and future perspectives

In this section I summarize all the work and give prospects for future work.

6.1 Conclusions

In this project, $Al_{0.95}CoFeNi_{2.05}$ EHEA was produced using PAAM. The resulting eutectic microstructure is very similar to that reported for other EHEAs of the same or similar composition. After numerous tensile experiments to determine its mechanical properties, its ductility exceeded that of conventionally cast EHEA. Subsequently, the deformation and fracture mechanisms of the PAAM HEA samples were studied. The following conclusions are achieved:

(1) The PAAM HEA exhibits distinct microstructural variations in its upper, middle, and lower sections. The top section consists of a lamellar-shaped B2 phase and a grid-shaped $L1_2$ phase, with $L1_2$ content at around 70%. In the middle part, both L_{12} and B2 phases are lamellar-shaped, each comprising approximately 50% of the structure. Towards the bottom, the $L1_2$ phase content sharply decreases while retaining its lamellar form. Conversely, the B2 phase rapidly expands and thickens into a grid shape. This change is associated with variations in Al content during the 3D printing process. Further investigations are ongoing to understand these changes better.

(2) The middle section of the HEA features a typical lamellar eutectic structure, with alternating soft $L1_2$ and hard B2 phases. The average thicknesses of the $L1_2$ and B2 lamellae are approximately 3.9 μm and 4.3 μm, respectively, with corresponding volume percentages of about 52.5% for $L1_2$ and 47.5% for B2. Notably, the removal of Cr in the customized eutectic composition results in the absence of nanoprecipitates in the B2 phase. The B2 phase is low in Co and Fe but rich in Ni and Al, while the $L1_2$ phase is only deficient in Al. Both phases contain similar amounts of Ni, but the B2 phase contains significantly more Ni than the $L1_2$ phase.

(3) HEA produced by PAAM exhibits excellent work hardening behavior. At the same time, HEA achieved a tensile ductility of approximately 24.5% and a high ultimate strength of approximately 960 MPa, which is more than twice the yield strength of approximately 450 MPa.

(4) To gain insights into the strong strain hardening observed in the 3D printed HEA, I conducted fracture analysis using SEM imaging techniques, including SE-SEM and BSE-SEM. Furthermore, I analyzed the material's fracture mechanism based on the strain-hardening rate. The final fracture pattern reveals a microstructure consisting of ductile and brittle fracture surfaces corresponding to the $L1_2$ and B2 phases, respectively.

6.2 Limitations and future research directions

Since the porosity of the sample itself is very high and the Al element is severely lost during the printing process, the mechanical properties of the sample are greatly affected. To optimize the mechanical properties of materials, subsequent work should start with material preparation methods. Solving the problem of excessive porosity in the printing process of PAAM technology and solving the problem of the disappearance of Al elements during the printing process will be the focus of subsequent work. At the same time, how to further improve the ductility of the material while the dendritic structure exists is also a problem faced by this material. Introducing disordered nanoscale ductile BCC and/or FCC phases into less flexible B2 intermetallic compounds is a solution worth investigating. Recent research by Yang et al. [116] has unveiled a strategy to enhance the ductility of ordered $L1_2$ -type intermetallic compounds. Disordered nanolayers positioned between adjacent micron-sized grains have been found to effectively address the poor ductility of these compounds [116]. These nanolayers act as a sustainable source of ductility, preventing brittle intergranular fracture by enhancing intragranular dislocation mobility. Therefore, the introduction of disordered nanoscale ductile BCC and/or FCC phases into less pliable B2 intermetallic compounds could

potentially serve as an alternative solution to improve ductility.

The well-known eutectic high entropy alloy (EHEA) features a balanced combination of strength and ductility, along with good fluidity and castability [70,97,140]. Furthermore, EHEAs have been reported to possess many additional attractive characteristics such as low interfacial energy, reduced notch sensitivity, high thermal stability, and appealing fatigue properties, to name a few [74,116,141−143]. The herringbone microstructure can also be realized in other bulk materials made up of hard and soft phases, thus enabling the design of materials that are resistant to cracking yet capable of high deformation. This is not accomplished by avoiding cracks but by guiding and cushioning them. Moreover, this method of designing a layered herringbone microstructure, and its significant impact on crack cushioning, not only promises to guide the design of new layered structural alloys with high elongation rates but also offers promising directions for designing novel bone substitute biomaterials with excellent fracture toughness.

$Al_{19}Fe_{20}Co_{20}Ni_{41}$ produced using the PAAM process boasts significant cost advantages and high ductility, along with the capability for creating materials with special appearances. Compared to most additive manufacturing technologies used for high entropy alloys (HEAs), PAAM offers the following benefits: First, the material costs are lower. Most additive manufacturing technologies require the pre-alloys, which are then ground into powder for printing. PAAM technology, on the other hand, allows for the direct printing of mechanically mixed powders, significantly saving both money and time. Second, similar to other additive manufacturing processes, it can produce parts of specific shapes. Third, it is well-known that some HEAs with a BCC structure have high hardness but low ductility. Meanwhile, HEAs containing FCC structures exhibit better ductility but lower hardness. Sometimes, HEAs cannot withstand the strength or the required ductility for the workpiece. Therefore, $Al_{19}Fe_{20}Co_{20}Ni_{41}$ can partially replace nickel-based superalloy coatings in a wide range of engineering applications that demand high strength, high ductility, and the manufacturing of parts with specific shapes, such as in aerospace, metallurgy, and machinery.

References

1. Kichloo, A. F., Raina, A., Haq, M. I. U., & Wani, M. S. (2021). Impact of carbon fiber reinforcement on mechanical and tribological behavior of 3D-Printed Polyethylene Terephthalate glycol Polymer Composites—An experimental investigation. *Journal of Materials Engineering and Performance*, *31*(2), 1021–1038. https://doi.org/10.1007/s11665-021-06262-6

2. Naveed, N. (2020). Investigate the effects of process parameters on material properties and microstructural changes of 3D-printed specimens using fused deposition modelling (FDM). *Materials Technology*, *36*(5), 317–330. https://doi.org/10.1080/10667857.2020.1758475

3. Jandyal, A., Chaturvedi, I., Wazir, I., Raina, A., & Haq, M. I. U. (2022). 3D printing – A review of processes, materials and applications in industry 4.0. *Sustainable Operations and Computers*, *3*, 33–42. https://doi.org/10.1016/j.susoc.2021.09.004

4. Tofail, S. a. M., Koumoulos, E. P., Bandyopadhyay, A., Bose, S., O'Donoghue, L. M., & Charitidis, C. A. (2018). Additive manufacturing: scientific and technological challenges, market uptake and opportunities. *Materials Today*, *21*(1), 22–37. https://doi.org/10.1016/j.mattod.2017.07.001

5. Shahrubudin, N., Lee, T., & Ramlan, R. (2019). An overview on 3D printing technology: technological, materials, and applications. *Procedia Manufacturing*, *35*, 1286–1296. https://doi.org/10.1016/j.promfg.2019.06.089

6. Keleş, Ö., Blevins, C. W., & Bowman, K. J. (2017). Effect of build orientation on the mechanical reliability of 3D printed ABS. *Rapid Prototyping Journal*, *23*(2), 320–328. https://doi.org/10.1108/rpj-09-2015-0122

7. Guo, N., & Leu, M. (2013). Additive manufacturing: technology, applications and research needs. *Frontiers of Mechanical Engineering*, *8*(3), 215–243. https://doi.org/10.1007/s11465-013-0248-8

8. Cantor, B., Chang, I., Knight, P. A., & Vincent, A. (2004). Microstructural development in equiatomic multicomponent alloys. *Materials Science and Engineering: A*, *375–377*, 213–218. https://doi.org/10.1016/j.msea.2003.10.257

9. Yeh, J., Chen, S., Lin, S., Gan, J., Chin, T., Shun, T., Tsau, C., & Chang, S. (2004). Nanostructured High-Entropy Alloys with Multiple Principal Elements: Novel Alloy Design Concepts and Outcomes. *Advanced Engineering Materials*, *6*(5), 299–303. https://doi.org/10.1002/adem.200300567

10. Ma, D., Tan, H., Zhang, Y., & Li, Y. (2003). Correlation between Glass Formation and Type of Eutectic Coupled Zone in Eutectic Alloys. *Materials Transactions*, *44*(10), 2007–2010. https://doi.org/10.2320/matertrans.44.2007

11. Zhang, Y., Yang, X., & Liaw, P. K. (2012). Alloy design and Properties Optimization of High-Entropy alloys. *JOM*, *64*(7), 830–838. https://doi.org/10.1007/s11837-012-0366-5

12. Yang, X., Zhang, Y., & Liaw, P. K. (2012). Microstructure and compressive properties of NBTIVTAALX high entropy alloys. *Procedia Engineering*, *36*, 292–298. https://doi.org/10.1016/j.proeng.2012.03.043

13. Zhang, Y., Wang, X. F., Chen, G. L., & Qiao, Y. (2006). Effect of ti on the microstructure and properties of CoCrCuFeNiTix high-entropy alloys. *European Journal of Control*. https://doi.org/10.3166/acsm.31.699-710

14. Yeh, J., Lin, S., Chin, T., Gan, J., Chen, S., Shun, T., Tsau, C., & Chou, S. (2004). Formation of simple crystal structures in Cu-Co-Ni-Cr-Al-Fe-Ti-V alloys with multiprincipal metallic elements. *Metallurgical and Materials Transactions*, *35*(8), 2533–2536. https://doi.org/10.1007/s11661-006-0234-4

15. Zhang, Y., Zuo, T. T., Tang, Z., Gao, M. C., Dahmen, K. A., Liaw, P. K., & Lu, Z. P. (2014). Microstructures and properties of high-entropy alloys. *Progress in Materials Science*, *61*, 1–93. https://doi.org/10.1016/j.pmatsci.2013.10.001

16. Ishengoma, F., & Mtaho, A. B. (2014). 3D Printing: Developing Countries perspectives. *International Journal of Computer Applications*, *104*(11), 30–34. https://doi.org/10.5120/18249-9329
17. Ovid'ko, I. A., Valiev, R. Z., & Zhu, Y. (2018). Review on superior strength and enhanced ductility of metallic nanomaterials. *Progress in Materials Science*, *94*, 462–540. https://doi.org/10.1016/j.pmatsci.2018.02.002
18. Hu, J., Shi, Y., Sauvage, X., Sha, G., & Lu, K. (2017). Grain boundary stability governs hardening and softening in extremely fine nanograined metals. *Science*, *355*(6331), 1292–1296. https://doi.org/10.1126/science.aal5166
19. Hahn, E. N., & Meyers, M. A. (2015). Grain-size dependent mechanical behavior of nanocrystalline metals. *Materials Science and Engineering: A*, *646*, 101–134. https://doi.org/10.1016/j.msea.2015.07.075
20. Buonassisi, T., Istratov, A. A., Pickett, M. D., Marcus, M. A., Ciszek, T., & Weber, E. R. (2006). Metal precipitation at grain boundaries in silicon: Dependence on grain boundary character and dislocation decoration. *Applied Physics Letters*, *89*(4). https://doi.org/10.1063/1.2234570
21. Lu, K. (2016). Stabilizing nanostructures in metals using grain and twin boundary architectures. *Nature Reviews Materials*, *1*(5). https://doi.org/10.1038/natrevmats.2016.19
22. Lasalmonie, A., & Strudel, J. (1986). Influence of grain size on the mechanical behaviour of some high strength materials. *Journal of Materials Science*, *21*(6), 1837–1852. https://doi.org/10.1007/bf00547918
23. Lim, H., Lee, M., Kim, J., Adams, B. L., & Wagoner, R. H. (2011). Simulation of polycrystal deformation with grain and grain boundary effects. *International Journal of Plasticity*, *27*(9), 1328–1354. https://doi.org/10.1016/j.ijplas.2011.03.001
24. Zhang, X. F., Fujita, T., Pan, D., Yu, J., Sakurai, T., & Chen, M. (2010). Influences of grain size and grain boundary segregation on mechanical behavior of nanocrystalline Ni. *Materials Science and Engineering: A*, *527*(9), 2297–2304. https://doi.org/10.1016/j.msea.2009.12.005

25. Arzt, E. (1998). Size effects in materials due to microstructural and dimensional constraints: a comparative review. *Acta Materialia*, *46*(16), 5611–5626. https://doi.org/10.1016/s1359-6454(98)00231-6
26. Beaudoin, A. J., Acharya, A., Chen, S. R., Korzekwa, D. R., & Stout, M. (2000). Consideration of grain-size effect and kinetics in the plastic deformation of metal polycrystals. *Acta Materialia*, *48*(13), 3409–3423. https://doi.org/10.1016/s1359-6454(00)00136-1
27. Sauvage, X., Wilde, G., Divinski, S. V., Horita, Z., & Valiev, R. Z. (2012). Grain boundaries in ultrafine grained materials processed by severe plastic deformation and related phenomena. *Materials Science and Engineering: A*, *540*, 1–12. https://doi.org/10.1016/j.msea.2012.01.080
28. Karakulak, E. (2019). A review: Past, present and future of grain refining of magnesium castings. *Journal of Magnesium and Alloys*, *7*(3), 355–369. https://doi.org/10.1016/j.jma.2019.05.001
29. Koch, C. C. (2007). Structural nanocrystalline materials: an overview. *Journal of Materials Science*, *42*(5), 1403–1414. https://doi.org/10.1007/s10853-006-0609-3
30. Yamashita, A., Horita, Z., & Langdon, T. G. (2001). Improving the mechanical properties of magnesium and a magnesium alloy through severe plastic deformation. *Materials Science and Engineering: A*, *300*(1–2), 142–147. https://doi.org/10.1016/s0921-5093(00)01660-9
31. Valiev, R. Z., & Langdon, T. G. (2006). Principles of equal-channel angular pressing as a processing tool for grain refinement. *Progress in Materials Science*, *51*(7), 881–981. https://doi.org/10.1016/j.pmatsci.2006.02.003
32. Han, S. Z., Choi, E., Lim, S. H., Kim, S., & Lee, J. (2021). Alloy design strategies to increase strength and its trade-offs together. *Progress in Materials Science*, *117*, 100720. https://doi.org/10.1016/j.pmatsci.2020.100720
33. Lewandowska, M., & Kurzydłowski, K. J. (2008). Recent development in grain refinement by hydrostatic extrusion. *Journal of Materials Science*, *43*(23–24), 7299–7306. https://doi.org/10.1007/s10853-008-2810-z

34. Wan, H., An, X., Kong, Q., Wu, X., Feng, W., Wang, H., Wu, J., Lü, C., Zha, W., Sun, H., & Huang, L. (2021). Fabrication of ultrafine grained FeCrAl-0.6 wt.% ZrC alloys with enhanced mechanical properties by spark plasma sintering. *Advanced Powder Technology*, *32*(5), 1380–1389. https://doi.org/10.1016/j.apt.2021.02.041

35. Edalati, K., Masuda, T., Arita, M., Furui, M., Sauvage, X., Horita, Z., & Valiev, R. Z. (2017). Room-Temperature superplasticity in an Ultrafine-Grained magnesium alloy. *Scientific Reports*, *7*(1). https://doi.org/10.1038/s41598-017-02846-2

36. Zhang, X. F., Fujita, T., Pan, D., Yu, J., Sakurai, T., & Chen, M. (2010). Influences of grain size and grain boundary segregation on mechanical behavior of nanocrystalline Ni. *Materials Science and Engineering: A*, *527*(9), 2297–2304. https://doi.org/10.1016/j.msea.2009.12.005

37. Arzt, E. (1998). Size effects in materials due to microstructural and dimensional constraints: a comparative review. *Acta Materialia*, *46*(16), 5611–5626. https://doi.org/10.1016/s1359-6454(98)00231-6

38. Beaudoin, A. J., Acharya, A., Chen, S. R., Korzekwa, D. R., & Stout, M. (2000). Consideration of grain-size effect and kinetics in the plastic deformation of metal polycrystals. *Acta Materialia*, *48*(13), 3409–3423. https://doi.org/10.1016/s1359-6454(00)00136-1

39. Sauvage, X., Wilde, G., Divinski, S. V., Horita, Z., & Valiev, R. Z. (2012). Grain boundaries in ultrafine grained materials processed by severe plastic deformation and related phenomena. *Materials Science and Engineering: A*, *540*, 1–12. https://doi.org/10.1016/j.msea.2012.01.080

40. Meyers, M. A., Mishra, A., & Benson, D. J. (2006). Mechanical properties of nanocrystalline materials. *Progress in Materials Science*, *51*(4), 427–556. https://doi.org/10.1016/j.pmatsci.2005.08.003

41. Morris, D. G., & Morris, C. F. (1996). Hardness, strength, ductility and toughness of nanocrystalline materials. *Materials Science Forum*, *235–238*, 861–872. https://doi.org/10.4028/www.scientific.net/msf.235-238.861

42. Suryanarayana, C. (1995). Nanocrystalline materials. *International Materials Reviews*, *40*(2), 41–64. https://doi.org/10.1179/imr.1995.40.2.41
43. Enayati, M., & Mohamed, F. A. (2014). Application of mechanical alloying/milling for synthesis of nanocrystalline and amorphous materials. *International Materials Reviews*, *59*(7), 394–416. https://doi.org/10.1179/1743280414y.0000000036
44. Fang, Z. Z., Wang, X., Ryu, T., Hwang, K. S., & Sohn, H. Y. (2009). Synthesis, sintering, and mechanical properties of nanocrystalline cemented tungsten carbide – A review. *International Journal of Refractory Metals & Hard Materials*, *27*(2), 288–299. https://doi.org/10.1016/j.ijrmhm.2008.07.011
45. Mao, Q., Liu, Y., & Zhao, Y. (2022). A review on mechanical properties and microstructure of ultrafine grained metals and alloys processed by rotary swaging. *Journal of Alloys and Compounds*, *896*, 163122. https://doi.org/10.1016/j.jallcom.2021.163122
46. Shao, C., Zhang, P., Zhu, Y., Zhang, Z., Tian, Y., & Zhang, Z. (2018). Simultaneous improvement of strength and plasticity: Additional work-hardening from gradient microstructure. *Acta Materialia*, *145*, 413–428. https://doi.org/10.1016/j.actamat.2017.12.028
47. Kang, L., & Chao, Y. (2019). A review on High-Strength Titanium Alloys: Microstructure, strengthening, and Properties. *Advanced Engineering Materials*, *21*(8). https://doi.org/10.1002/adem.201801359
48. Hajalilou, A., & Mazlan, S. A. (2016). A review on preparation techniques for synthesis of nanocrystalline soft magnetic ferrites and investigation on the effects of microstructure features on magnetic properties. *Applied Physics A*, *122*(7). https://doi.org/10.1007/s00339-016-0217-2
49. Guillon, O., González-Julián, J., Dargatz, B., Kessel, T., Schierning, G., Räthel, J., & Herrmann, M. (2014). Field-Assisted Sintering Technology/Spark Plasma Sintering: Mechanisms, materials, and technology developments. *Advanced Engineering Materials*, *16*(7), 830–849. https://doi.org/10.1002/adem.201300409

50. Ahmadi, M., Tabary, S. B., Rahmatabadi, D., Ebrahimi, M., Abrinia, K., & Hashemi, R. (2022). Review of selective laser melting of magnesium alloys: advantages, microstructure and mechanical characterizations, defects, challenges, and applications. *Journal of Materials Research and Technology*, *19*, 1537–1562. https://doi.org/10.1016/j.jmrt.2022.05.102
51. Liu, Z., Zhao, D., Wang, P., Yan, M., Yang, C., Chen, Z., Lü, J., & Liu, X. (2022). Additive manufacturing of metals: Microstructure evolution and multistage control. *Journal of Materials Science & Technology*, *100*, 224–236. https://doi.org/10.1016/j.jmst.2021.06.011
52. Aboulkhair, N. T., Simonelli, M., Parry, L. A., Ashcroft, I., Tuck, C., & Hague, R. (2019). 3D printing of Aluminium alloys: Additive Manufacturing of Aluminium alloys using selective laser melting. *Progress in Materials Science*, *106*, 100578. https://doi.org/10.1016/j.pmatsci.2019.100578
53. Sigworth, G. K., & Kuhn, T. A. (2007). Grain refinement of aluminum casting alloys. *International Journal of Metalcasting*, *1*(1), 31–40. https://doi.org/10.1007/bf03355416
54. Metan, V., Eigenfeld, K., Räbiger, D., Leonhardt, M., & Eckert, S. (2009). Grain size control in Al–Si alloys by grain refinement and electromagnetic stirring. *Journal of Alloys and Compounds*, *487*(1–2), 163–172. https://doi.org/10.1016/j.jallcom.2009.08.032
55. StJohn, D. H., Easton, M., Qian, M., & Taylor, J. A. (2012). Grain refinement of magnesium alloys: A review of recent research, theoretical developments, and their application. *Metallurgical and Materials Transactions*, *44*(7), 2935–2949. https://doi.org/10.1007/s11661-012-1513-x
56. Birol, Y. (2013). Impact of grain size on mechanical properties of AlSi7Mg0.3 alloy. *Materials Science and Engineering: A*, *559*, 394–400. https://doi.org/10.1016/j.msea.2012.08.115
57. Murty, B., Kori, S., & Chakraborty, M. (2002). Grain refinement of aluminium and its alloys by heterogeneous nucleation and alloying. *International Materials Reviews*, *47*(1), 3–29. https://doi.org/10.1179/095066001225001049

58. Todaro, C. J., Easton, M., Qiu, D., Zhang, D., Bermingham, M., Lui, E., Brandt, M., StJohn, D. H., & Qian, M. (2020). Grain structure control during metal 3D printing by high-intensity ultrasound. *Nature Communications*, *11*(1). https://doi.org/10.1038/s41467-019-13874-z

59. Kuo, C., Chua, C. K., Peng, P. C., Chen, Y. W., Sing, S. L., Huang, S., & Su, Y. (2019). Microstructure evolution and mechanical property response via 3D printing parameter development of Al–Sc alloy. *Virtual and Physical Prototyping*, *15*(1), 120–129. https://doi.org/10.1080/17452759.2019.1698967

60. Han, C., Fang, Q., Shi, Y., Tor, S. B., Chua, C. K., & Zhou, K. (2020). Recent advances on High-Entropy alloys for 3D printing. *Advanced Materials*, *32*(26). https://doi.org/10.1002/adma.201903855

61. Martin, J. H., Yahata, B. D., Hundley, J. M., Mayer, J., Schaedler, T. A., & Pollock, T. M. (2017). 3D printing of high-strength aluminium alloys. *Nature*, *549*(7672), 365–369. https://doi.org/10.1038/nature23894

62. Li, Z., Liu, C., Wang, B., Wang, C., Wang, Z., Yang, F., Gao, C., Li, H., & Qin, Y. (2018). Heat treatment effect on the mechanical properties, roughness and bone ingrowth capacity of 3D printing porous titanium alloy. *RSC Advances*, *8*(22), 12471–12483. https://doi.org/10.1039/c7ra13313h

63. Yang, C., Tian, X., Li, D., Cao, Y., Feng, Z., & Shi, C. (2017). Influence of thermal processing conditions in 3D printing on the crystallinity and mechanical properties of PEEK material. *Journal of Materials Processing Technology*, *248*, 1–7. https://doi.org/10.1016/j.jmatprotec.2017.04.027

64. Guo, Y., Jia, L., Kong, B., Peng, H., & Zhang, H. (2017). Heat treatment induced phase transition and microstructural evolution in electron beam surface melted Nb-Si based alloys. *Applied Surface Science*, *423*, 417–420. https://doi.org/10.1016/j.apsusc.2017.05.248

65. Roudnická, M., Bigas, J., Molnárová, O., Paloušek, D., & Vojtěch, D. (2021). Different response of cast and 3D-Printed Co-CR-MO alloy to heat treatment: a thorough microstructure characterization. *Metals*, *11*(5), 687. https://doi.org/10.3390/met11050687

66. Gu, D., Ma, Z., Li, X., Shen, Z., Guo, S., Zhang, H., Cheng, X., & Cai, H. (2023). Designing (TiZrHf)100-xCux high entropy alloys with abnormal as-cast divorced eutectoid microstructure and balanced mechanical properties. *Materials Science and Engineering: A*, *879*, 145217. https://doi.org/10.1016/j.msea.2023.145217

67. Yang, L., Jiang, X., Sun, H., Shao, Z., Fang, Y., & Shu, R. (2021). Effects of alloying, heat treatment and nanoreinforcement on mechanical properties and damping performances of Cu–Al-based alloys: A review. *Nanotechnology Reviews*, *10*(1), 1560–1591. https://doi.org/10.1515/ntrev-2021-0101

68. TMS 2020 149th Annual Meeting & Exhibition Supplemental Proceedings. (2020). In *The minerals, metals & materials series*. https://doi.org/10.1007/978-3-030-36296-6

69. Chanda, B., Potnis, G., Jana, P. P., & Das, J. (2020). A review on nano-/ultrafine advanced eutectic alloys. *Journal of Alloys and Compounds*, *827*, 154226. https://doi.org/10.1016/j.jallcom.2020.154226

70. Lu, Y., Dong, Y., Guo, S., Jiang, L., Kang, H., Wang, T., Wen, B., Wang, Z., Jie, J., Cao, Z., Ruan, H., & Li, T. (2014). A promising new class of High-Temperature alloys: Eutectic High-Entropy alloys. *Scientific Reports*, *4*(1). https://doi.org/10.1038/srep06200

71. Jiang, L., Lu, Y., Dong, Y., Wang, T., Cao, Z., & Li, T. (2015). Effects of Nb addition on structural evolution and properties of the CoFeNi2V0.5 high-entropy alloy. *Applied Physics A*, *119*(1), 291–297. https://doi.org/10.1007/s00339-014-8964-4

72. Shi, P., Li, R., Li, Y., Wen, Y., Zhong, Y., Ren, W., Shen, Z., Zheng, T., Peng, J., Li, X., Hu, P., Min, N., Zhang, Y., Ren, Y., Liaw, P. K., Raabe, D., & Wang, Y. (2021). Hierarchical crack buffering triples ductility in eutectic herringbone high-entropy alloys. *Science*, *373*(6557), 912–918. https://doi.org/10.1126/science.abf6986

73. Wu, Q., Wang, Z., Hu, X., Zheng, T., Yang, Z., He, F., Li, J., & Wang, J. (2020). Uncovering the eutectics design by machine learning in the Al–Co–Cr–Fe–Ni high

entropy system. *Acta Materialia*, *182*, 278–286. https://doi.org/10.1016/j.actamat.2019.10.043

74. Xiong, T., Yang, W., Zheng, S., Liu, Z., Lu, Y., Zhang, R., Zhou, Y., Shao, X., Zhang, B., Wang, J., Yin, F., Liaw, P. K., & Ma, X. (2021). Faceted Kurdjumov-Sachs interface-induced slip continuity in the eutectic high-entropy alloy, AlCoCrFeNi2.1. *Journal of Materials Science & Technology*, *65*, 216–227. https://doi.org/10.1016/j.jmst.2020.04.073
75. Fidan, I., Huseynov, O., Ali, M. A., Alkunte, S., Rajeshirke, M., Gupta, A., Hasanov, S., Tantawi, K., Yasa, E., Yılmaz, O., Loy, J., Popov, V. V., & Popov, V. V. (2023). Recent inventions in additive Manufacturing: Holistic review. *Inventions*, *8*(4), 103. https://doi.org/10.3390/inventions8040103
76. Gu, D. (2015). Laser Additive Manufacturing of High-Performance Materials. In *Springer eBooks*. https://doi.org/10.1007/978-3-662-46089-4
77. Katz-Demyanetz, A., Popov, V. V., Kovalevsky, A. A., Safranchik, D., & Koptyug, A. (2019). Powder-bed additive manufacturing for aerospace application: Techniques, metallic and metal/ceramic composite materials and trends. *Manufacturing Review*, *6*, 5. https://doi.org/10.1051/mfreview/2019003
78. Khorasani, M., Ghasemi, A., Rolfe, B., & Gibson, I. (2021b). Additive manufacturing a powerful tool for the aerospace industry. *Rapid Prototyping Journal*, *28*(1), 87–100. https://doi.org/10.1108/rpj-01-2021-0009
79. Tepylo, N., Huang, X., & Patnaik, P. C. (2019). Laser-Based additive manufacturing technologies for aerospace applications. *Advanced Engineering Materials*, *21*(11). https://doi.org/10.1002/adem.201900617
80. Yuan, S., Shen, F., Chua, C. K., & Zhou, K. (2019). Polymeric composites for powder-based additive manufacturing: Materials and applications. *Progress in Polymer Science*, *91*, 141–168. https://doi.org/10.1016/j.progpolymsci.2018.11.001
81. Camacho, D. D., Clayton, P. M., O'Brien, W. J., Seepersad, C. C., Juenger, M., Ferron, R. D., & Salamone, S. (2018). Applications of additive manufacturing in

the construction industry – A forward-looking review. *Automation in Construction*, *89*, 110–119. https://doi.org/10.1016/j.autcon.2017.12.031

82. Bandyopadhyay, A., & Heer, B. (2018). Additive manufacturing of multi-material structures. *Materials Science and Engineering: R: Reports*, *129*, 1–16. https://doi.org/10.1016/j.mser.2018.04.001
83. Zhang, Y., Zhou, Y., Lin, J., Chen, G. L., & Liaw, P. K. (2008). Solid-Solution phase formation rules for multi-component alloys. *Advanced Engineering Materials*, *10*(6), 534–538. https://doi.org/10.1002/adem.200700240
84. Li, C., Li, J., Zhao, M., & Jiang, Q. (2009). Effect of alloying elements on microstructure and properties of multiprincipal elements high-entropy alloys. *Journal of Alloys and Compounds*, *475*(1–2), 752–757. https://doi.org/10.1016/j.jallcom.2008.07.124
85. Zhang, Y. (2010). Mechanical properties and structures of high entropy alloys and bulk metallic glasses composites. *Materials Science Forum*, *654–656*, 1058–1061. https://doi.org/10.4028/www.scientific.net/msf.654-656.1058
86. Zhang, H., Pan, Y., He, Y., & Jiao, H. (2011). Microstructure and properties of 6FeNiCoSiCrAlTi high-entropy alloy coating prepared by laser cladding. *Applied Surface Science*, *257*(6), 2259–2263. https://doi.org/10.1016/j.apsusc.2010.09.084
87. Lin, C., Tsai, H., & Bor, H. (2010). Effect of aging treatment on microstructure and properties of high-entropy Cu0.5CoCrFeNi alloy. *Intermetallics*, *18*(6), 1244–1250. https://doi.org/10.1016/j.intermet.2010.03.030
88. Yeh, J. W., Chen, Y. L., Lin, S., & Chen, S. K. (2007). High-Entropy Alloys – A New Era of Exploitation. *Materials Science Forum*, *560*, 1–9. https://doi.org/10.4028/www.scientific.net/msf.560.1
89. Sharma, P., Dwivedi, V. K., & Dwivedi, S. P. (2021). Development of high entropy alloys: A review. *Materials Today: Proceedings*, *43*, 502–509. https://doi.org/10.1016/j.matpr.2020.12.023
90. Bernal, J. D., Bunn, C., Lonsdale, D., & James, R. W. (1962). British and Commonwealth Schools of Crystallography. In *Springer eBooks* (pp. 374–429). https://doi.org/10.1007/978-1-4615-9961-6_30

91. Heirs of the revolution: X-ray diffraction and the birth of the Mineralogical Society of America. (2020). *American Mineralogist*. https://doi.org/10.2138/am-2019-7205
92. Liu, X., Wang, H., Chen, L., Baker, I., Yeh, J., Liu, C., & Nieh, T. (2015). An assessment on the future development of high-entropy alloys: Summary from a recent workshop. *Intermetallics*, *66*, 67–76. https://doi.org/10.1016/j.intermet.2015.06.021
93. George, E., Raabe, D., & Ritchie, R. O. (2019). High-entropy alloys. *Nature Reviews Materials*, *4*(8), 515–534. https://doi.org/10.1038/s41578-019-0121-4
94. Lu, Y., Dong, Y., Jiang, H., Wang, Z., Cao, Z., Guo, S., Wang, T., Li, T., & Liaw, P. K. (2020). Promising properties and future trend of eutectic high entropy alloys. *Scripta Materialia*, *187*, 202–209. https://doi.org/10.1016/j.scriptamat.2020.06.022
95. Horckmans, L., Möckel, R., Nielsen, P., Kukurugya, F., Vanhoof, C., Morillon, A., & Algermissen, D. (2019). Multi-Analytical characterization of SLAGS to determine the chromium concentration for a possible Re-Extraction. *Minerals*, *9*(10), 646. https://doi.org/10.3390/min9100646
96. Shi, P., Ren, W., Zheng, T., Ren, Z., Hou, X., Peng, J., Hu, P., Gao, Y., Zhong, Y., & Liaw, P. K. (2019). Enhanced strength–ductility synergy in ultrafine-grained eutectic high-entropy alloys by inheriting microstructural lamellae. *Nature Communications*, *10*(1). https://doi.org/10.1038/s41467-019-08460-2
97. Lu, Y., Gao, X., Jiang, L., Chen, Z., Wang, T., Jie, J., Kang, H., Zhang, Y., Guo, S., Ruan, H., Zhao, Y., Cao, Z., & Li, T. (2017). Directly cast bulk eutectic and near-eutectic high entropy alloys with balanced strength and ductility in a wide temperature range. *Acta Materialia*, *124*, 143–150. https://doi.org/10.1016/j.actamat.2016.11.016
98. Goldstein, J. I., Newbury, D. E., Michael, J. R., Ritchie, N. W. M., Scott, J. H. J., & Joy, D. C. (2018). Scanning electron microscopy and X-Ray microanalysis. In *Springer eBooks*. https://doi.org/10.1007/978-1-4939-6676-9
99. Yang, G., & Kim, J. (2022). Hierarchical precipitates, sequential deformation-induced phase transformation, and enhanced back stress strengthening of the micro-

alloyed high entropy alloy. *Acta Materialia*, *233*, 117974. https://doi.org/10.1016/j.actamat.2022.117974

100. Dong, B., Wang, Z., Pan, Z., Muránsky, O., Shen, C., Reid, M., Chen, X., & Li, H. (2021). On the development of pseudo-eutectic AlCoCrFeNi2.1 high entropy alloy using Powder-bed Arc Additive Manufacturing (PAAM) process. *Materials Science and Engineering: A*, *802*, 140639. https://doi.org/10.1016/j.msea.2020.140639

101. McDonald, S. D., Nogita, K., & Dahle, A. K. (2006). Eutectic grain size and strontium concentration in hypoeutectic aluminium–silicon alloys. *Journal of Alloys and Compounds*, *422*(1–2), 184–191. https://doi.org/10.1016/j.jallcom.2005.11.070

102. Jin, X., Bi, J., Zhang, L., Zhou, Y., Du, X., Liang, Y., & Li, B. (2019). A new CrFeNi2Al eutectic high entropy alloy system with excellent mechanical properties. *Journal of Alloys and Compounds*, *770*, 655–661. https://doi.org/10.1016/j.jallcom.2018.08.176

103. Lim, K. R., Kwon, H. J., Kang, J., Won, J. W., & Na, Y. S. (2020). A novel ultra-high-strength duplex Al–Co–Cr–Fe–Ni high-entropy alloy reinforced with body-centered-cubic ordered-phase particles. *Materials Science and Engineering: A*, *771*, 138638. https://doi.org/10.1016/j.msea.2019.138638

104. Nguyen, T., Huang, M., Li, H., Tran, V., & Yang, S. (2021). Microstructure and tensile properties of duplex phase Al0.25FeMnNiCrCu0.5 high entropy alloy fabricated by laser melting deposition. *Journal of Alloys and Compounds*, *871*, 159521. https://doi.org/10.1016/j.jallcom.2021.159521

105. Shi, P., Li, R., Li, Y., Wen, Y., Zhong, Y., Ren, W., Shen, Z., Zheng, T., Peng, J., Li, X., Hu, P., Min, N., Zhang, Y., Ren, Y., Liaw, P. K., Raabe, D., & Wang, Y. (2021). Hierarchical crack buffering triples ductility in eutectic herringbone high-entropy alloys. *Science*, *373*(6557), 912–918. https://doi.org/10.1126/science.abf6986

106. Yang, G., & Kim, J. (2022). Hierarchical precipitates, sequential deformation-induced phase transformation, and enhanced back stress strengthening of the micro-

alloyed high entropy alloy. *Acta Materialia*, *233*, 117974. https://doi.org/10.1016/j.actamat.2022.117974

107. Yeh, J., Chen, S., Lin, S., Gan, J., Chin, T., Shun, T., Tsau, C., & Chang, S. (2004d). Nanostructured High-Entropy Alloys with Multiple Principal Elements: Novel Alloy Design Concepts and Outcomes. *Advanced Engineering Materials*, *6*(5), 299–303. https://doi.org/10.1002/adem.200300567

108. Ding, Z., He, Q., Chung, D. Y., & Yang, Y. (2020). Evading brittle fracture in submicron-sized high entropy intermetallics in dual-phase eutectic microstructure. *Scripta Materialia*, *187*, 280–284. https://doi.org/10.1016/j.scriptamat.2020.06.032

109. Jiang, H., Qiao, D., Jiao, W., Han, K., Lu, Y., & Liaw, P. K. (2021). Tensile deformation behavior and mechanical properties of a bulk cast Al0.9CoFeNi2 eutectic high-entropy alloy. *Journal of Materials Science & Technology*, *61*, 119–124. https://doi.org/10.1016/j.jmst.2020.05.053

110. Huo, W., Zhou, H., Fang, F., Xie, Z., & Jiang, J. (2017). Microstructure and mechanical properties of CoCrFeNiZrx eutectic high-entropy alloys. *Materials & Design*, *134*, 226–233. https://doi.org/10.1016/j.matdes.2017.08.030

111. Ding, Z., He, Q., Wang, Q., & Yang, Y. (2018). Superb strength and high plasticity in laves phase rich eutectic medium-entropy-alloy nanocomposites. *International Journal of Plasticity*, *106*, 57–72. https://doi.org/10.1016/j.ijplas.2018.03.001

112. Tan, Y. K., Li, J., Wang, J., & Kou, H. (2019). Effect of MN addition on the microstructures and mechanical properties of COCRFENIPD High entropy alloy. *Entropy*, *21*(3), 288. https://doi.org/10.3390/e21030288

113. Jin, X., Zhou, Y., Zhang, L., Du, X., & Li, B. (2018). A new pseudo binary strategy to design eutectic high entropy alloys using mixing enthalpy and valence electron concentration. *Materials & Design*, *143*, 49–55. https://doi.org/10.1016/j.matdes.2018.01.057

114. Han, L., Xu, X., Wang, L., Pyczak, F., Zhou, R., & Liu, Y. (2019). A eutectic high-entropy alloy with good high-temperature strength-plasticity balance.

Materials Research Letters, *7*(11), 460–466. https://doi.org/10.1080/21663831.2019.1650130

115. Xiong, T., Zheng, S., Pang, J., & Ma, X. (2020). High-strength and high-ductility AlCoCrFeNi2.1 eutectic high-entropy alloy achieved via precipitation strengthening in a heterogeneous structure. *Scripta Materialia*, *186*, 336–340. https://doi.org/10.1016/j.scriptamat.2020.04.035

116. Shi, P., Li, Y., Wen, Y., Li, Y., Wang, Y., Ren, W., Zheng, T., Guo, Y., Hou, L., Shen, Z., Jiang, Y., Peng, J., Hu, P., Liang, N., Liu, Q., & Liaw, P. K. (2021). A precipitate-free AlCoFeNi eutectic high-entropy alloy with strong strain hardening. *Journal of Materials Science & Technology*, *89*, 88–96. https://doi.org/10.1016/j.jmst.2021.03.005

117. Dong, Y., Yao, Z., Huang, X., Du, F., Li, C., Chen, A., Wu, F., Cheng, Y., & Zhang, Z. (2020). Microstructure and mechanical properties of AlCoxCrFeNi3-x eutectic high-entropy-alloy system. *Journal of Alloys and Compounds*, *823*, 153886. https://doi.org/10.1016/j.jallcom.2020.153886

118. Wang, L., Shen, J., Shang, Z., & Fu, H. (2014). Microstructure evolution and enhancement of fracture toughness of NiAl–Cr(Mo)–(Hf,Dy) alloy with a small addition of Fe during heat treatment. *Scripta Materialia*, *89*, 1–4. https://doi.org/10.1016/j.scriptamat.2014.07.002

119. Wu, Q., Wang, Z., Zheng, T., Chen, D., Yang, Z., Li, J., Kai, J., & Wang, J. (2019). A casting eutectic high entropy alloy with superior strength-ductility combination. *Materials Letters*, *253*, 268–271. https://doi.org/10.1016/j.matlet.2019.06.067

120. Gutiérrez-Urrutia, I., & Raabe, D. (2011). Dislocation and twin substructure evolution during strain hardening of an Fe–22wt.% Mn–0.6wt.% C TWIP steel observed by electron channeling contrast imaging. *Acta Materialia*, *59*(16), 6449–6462. https://doi.org/10.1016/j.actamat.2011.07.009

121. Cao, R., Yu, Q., Pan, J., Lin, Y., Sweet, A., Li, Y., & Ritchie, R. O. (2020). On the exceptional damage-tolerance of gradient metallic materials. *Materials Today*, *32*, 94–107. https://doi.org/10.1016/j.mattod.2019.09.023

122. Mäder, S., Seeger, A., & Leitz, C. (1963). Work Hardening and Dislocation Arrangement of fcc Single Crystals. I. Plastic Deformation and Slip Line Studies of Nickel Single Crystals. *Journal of Applied Physics*, *34*(11), 3368–3375. https://doi.org/10.1063/1.1729194

123. Wei, S., Kim, S. J., Kang, J. H., Zhang, Y., Zhang, Y., Furuhara, T., Park, E. S., & Taşan, C. C. (2020). Natural-mixing guided design of refractory high-entropy alloys with as-cast tensile ductility. *Nature Materials*, *19*(11), 1175–1181. https://doi.org/10.1038/s41563-020-0750-4

124. Wei, S., Kim, S. J., Kang, J. H., Zhang, Y., Zhang, Y., Furuhara, T., Park, E. S., & Taşan, C. C. (2020). Natural-mixing guided design of refractory high-entropy alloys with as-cast tensile ductility. *Nature Materials*, *19*(11), 1175–1181. https://doi.org/10.1038/s41563-020-0750-4

125. Gao, X., Lu, Y., Liu, J., Wang, J., Wang, T., & Zhao, Y. (2019). Extraordinary ductility and strain hardening of Cr26Mn20Fe20Co20Ni14 TWIP high-entropy alloy by cooperative planar slipping and twinning. *Materialia*, *8*, 100485. https://doi.org/10.1016/j.mtla.2019.100485

126. Welsch, E. D., Ponge, D., Haghighat, S. M. H., Sandlöbes, S., Choi, P., Herbig, M., Zaefferer, S., & Raabe, D. (2016). Strain hardening by dynamic slip band refinement in a high-Mn lightweight steel. *Acta Materialia*, *116*, 188–199. https://doi.org/10.1016/j.actamat.2016.06.037

127. Liu, C., Stringer, J., Mundy, J. N., Horton, L., & Angelini, P. (1997). Ordered intermetallic alloys: an assessment. *Intermetallics*, *5*(8), 579–596. https://doi.org/10.1016/s0966-9795(97)00045-9

128. Jiao, Z., Luan, J., & Liu, C. T. (2016). Strategies for improving ductility of ordered intermetallics. *Progress in Natural Science: Materials International*, *26*(1), 1–12. https://doi.org/10.1016/j.pnsc.2016.01.014

129. Yang, T., Zhao, Y., Li, W., Yu, C., Luan, J., Lin, D., Fan, L., Jiao, Z., Wh, L., X-j, L., Kai, J. J., Huang, J., & Ct, L. (2020). Ultrahigh-strength and ductile superlattice alloys with nanoscale disordered interfaces. *Science*, *369*(6502), 427–432. https://doi.org/10.1126/science.abb6830

130. Huang, C., Hu, C., Liu, Y., Liang, Z., & Huang, M. (2022). Recent developments and perspectives of advanced high-strength medium Mn steel: from material design to failure mechanisms. *Materials Futures*, *1*(3), 032001. https://doi.org/10.1088/2752-5724/ac7fae

131. Yang, Z., Wang, Z. J., Wu, Q., Zheng, T., Zhao, P., Zhao, J., & Chen, J. (2019). Enhancing the mechanical properties of casting eutectic high entropy alloys with Mo addition. *Applied Physics A*, *125*(3). https://doi.org/10.1007/s00339-019-2506-z

132. Jin, X., Liang, Y., Bi, J., & Li, B. (2020). Enhanced strength and ductility of Al0.9CoCrNi2.1 eutectic high entropy alloy by thermomechanical processing. *Materialia*, *10*, 100639. https://doi.org/10.1016/j.mtla.2020.100639

133. Ma, L., Wang, J., & Jin, P. (2020). Microstructure and mechanical properties variation with Ni content in $Al_{0.8}CoCr_{0.6}Fe_{0.7}Ni_x$ (x = 1.1, 1.5, 1.8, 2.0) eutectic high-entropy alloy system. *Materials Research Express*, *7*(1), 016566. https://doi.org/10.1088/2053-1591/ab6580

134. Koyama, M., Zhang, Z., Wang, M., Ponge, D., Raabe, D., Tsuzaki, K., Noguchi, H., & Taşan, C. C. (2017). Bone-like crack resistance in hierarchical metastable nanolaminate steels. *Science*, *355*(6329), 1055–1057. https://doi.org/10.1126/science.aal2766

135. Liu, L., Yu, Q., Wang, Z., Ell, J., Huang, M., & Ritchie, R. O. (2020). Making ultrastrong steel tough by grain-boundary delamination. *Science*, *368*(6497), 1347–1352. https://doi.org/10.1126/science.aba9413

136. Huang, C., Hu, C., Liu, Y., Liang, Z., & Huang, M. (2022). Recent developments and perspectives of advanced high-strength medium Mn steel: from material design to failure mechanisms. *Materials Futures*, *1*(3), 032001. https://doi.org/10.1088/2752-5724/ac7fae

137. Sun, B., Palanisamy, D., Ponge, D., Gault, B., Fazeli, F., Scott, C., Yue, S., & Raabe, D. (2019). Revealing fracture mechanisms of medium manganese steels with and without delta-ferrite. *Acta Materialia*, *164*, 683–696. https://doi.org/10.1016/j.actamat.2018.11.029

138. Yan, D., Taşan, C. C., & Raabe, D. (2015). High resolution in situ mapping of microstrain and microstructure evolution reveals damage resistance criteria in dual phase steels. *Acta Materialia*, *96*, 399–409. https://doi.org/10.1016/j.actamat.2015.05.038

139. Alaie, A., Kadkhodapour, J., Rad, S. Z., Asadabad, M. A., & Schmauder, S. (2015). Formation and coalescence of strain localized regions in ferrite phase of DP600 steels under uniaxial tensile deformation. *Materials Science and Engineering: A*, *623*, 133–144. https://doi.org/10.1016/j.msea.2014.11.042

140. Gao, X., Lu, Y., Zhang, B., Liang, N., Wu, G., Sha, G., & Liu, J. (2017). Microstructural origins of high strength and high ductility in an AlCoCrFeNi2.1 eutectic high-entropy alloy. *Acta Materialia*, *141*, 59–66. https://doi.org/10.1016/j.actamat.2017.07.041

141. Zhang, W., Liu, L., Peng, S., Ren, J., Wu, F. F., Shang, J. K., Chen, M., Zhang, Y., Zhao, Z., Qi, J., Wang, B., & Chen, W. (2021). The tensile property and notch sensitivity of AlCoCrFeNi2.1 high entropy alloy with a novel "steel-frame" eutectic microstructure. *Journal of Alloys and Compounds*, *863*, 158747. https://doi.org/10.1016/j.jallcom.2021.158747

142. Jiang, H., Qiao, D., Lu, Y., Ren, Z., Cao, Z., Wang, T., & Li, T. (2019). Direct solidification of bulk ultrafine-microstructure eutectic high-entropy alloys with outstanding thermal stability. *Scripta Materialia*, *165*, 145–149. https://doi.org/10.1016/j.scriptamat.2019.02.035

143. Shukla, S., Wang, T., Cotton, S., & Mishra, R. S. (2018). Hierarchical microstructure for improved fatigue properties in a eutectic high entropy alloy. *Scripta Materialia*, *156*, 105–109. https://doi.org/10.1016/j.scriptamat.2018.07.022